FEATURE ARTICLE

Physicochemical Properties of Nitrate Aerosols: Implications for the Atmosphere

Elizabeth R. Gibson,[†] Paula K. Hudson,[‡] and Vicki H. Grassian*[,†,‡]

Department of Chemistry and the Center for Global and Environmental Research, The University of Iowa, Iowa City, Iowa 52242

Received: June 19, 2006; In Final Form: August 8, 2006

As aerosols, such as sea salt and mineral dust, are transported through the atmosphere they undergo heterogeneous reactions with nitrogen oxides to form nitrate salts. The nitrate salt can have quite different physicochemical properties than the original aerosol, resulting in an aerosol that will markedly differ in its climate impact, heterogeneous chemistry, and photoactivity. In this Feature Article, we will review some aspects of the importance of aqueous nitrate aerosols as well as describe a new multi-analysis aerosol reactor system (MAARS) that is used to measure the physicochemical properties of these atmospherically relevant aerosols. Here we show measurements of the hygroscopic properties, cloud condensation nuclei activity, and FTIR extinction of nitrate salt aerosol. In particular, we have measured the hygroscopic growth of 100 nm size-selected nitrate particles including $NaNO_3$, $Ca(NO_3)_2$, $Mg(NO_3)_2$, and a 1:1 mixture of $Ca(NO_3)_2$ and $Mg(NO_3)_2$ as a function of relative humidity (*RH*) at 298 K. Using Köhler theory, we have quantified the water content of these particles with increasing *RH*. FTIR extinction measurements of the full size distribution of each of the nitrate aerosols are analyzed to yield information about the local solvation environment of the nitrate ions and the long-wavelength light scattering of the particles at different *RH*. Furthermore, we have measured and compared the cloud condensation nuclei (CCN) activity of $CaCO_3$, a large component of mineral dust aerosol, and $Ca(NO_3)_2$, a product of atmospherically aged $CaCO_3$ through reaction with nitrogen oxides, at supersaturations from 0.1% to 0.9%. These quantitative physicochemical data are needed if we are to better understand the chemistry as well as the climate effects of atmospheric aerosols as they are entrained, transported, reacted, and aged in the atmosphere. Our studies here focus on aqueous nitrate salts, the products of the reaction of nitrogen oxides with sea salt and mineral dust aerosol.

Introduction

Atmospheric aerosols such as sea salt and mineral dust are an important component of the Earth's atmosphere.[1,2] Sea salt aerosol, produced from wave action, and mineral dust aerosol, produced from wind blown soils, can be entrained in the atmosphere for days to weeks. Both sea salt and mineral dust particles have highly reactive surfaces that undergo heterogeneous chemistry as they are transported through polluted environments in the atmosphere.[3−10] In particular, sea salt and mineral dust aerosol react with nitrogen oxides including NO_2, NO_3, HNO_3 and N_2O_5, to yield nitrate salt products.[5,11]

It is well known that nitrogen oxides undergo heterogeneous reactions with NaCl, a major component of sea salt, via the following chemical reaction pathways:

$$NaCl\ (s,aq) + HNO_3\ (g) \xrightarrow{\%\ RH} NaNO_3\ (s,aq) + HCl\ (g) \quad (1)$$

$$NaCl\ (s,aq) + N_2O_5\ (g) \xrightarrow{\%\ RH} NaNO_3\ (s,aq) + ClNO_2\ (g) \quad (2)$$

$$NaCl\ (s,aq) + 2NO_2\ (g) \xrightarrow{\%\ RH} NaNO_3\ (s,aq) + ClNO\ (g) \quad (3)$$

where the state of the aerosol, solid (s) or aqueous liquid (aq), will depend on the relative humidity.

The heterogeneous uptake coefficient (γ) for the reaction of HNO_3 and N_2O_5 on NaCl has been measured to be $(1.0 \pm 0.8) \times 10^{-3}$ and $(2.9 \pm 1.7) \times 10^{-3}$, respectively, by Hoffman et al. in single layer particle studies.[12,13] Diffuse reflectance FTIR analysis has shown $NaNO_3$ product formation as NaCl particles are exposed to these gases.[14] $NaNO_3$ is more hygroscopic than NaCl over a large range of relative humidities but not as hygroscopic as sea salt itself, which is a multicomponent aerosol with a composition of Na_1, $Mg_{0.11}$, $Ca_{0.02}$, $K_{0.02}$, $Cl_{1.16}$, $S_{0.06}$, and $Br_{0.002}$ (mole ratios).[2,11,15] Because of the multicomponent nature of sea salt, there are other potential reactions with HNO_3 that may form nitrate salts, including the following reaction with $MgCl_2$:

* To whom correspondence should be addressed. E-mail: vicki-grassian@uiowa.edu. Tel: 319-335-1392. Fax: 319-353-1115.
† Department of Chemistry.
‡ Center for Global and Environmental Research.

10.1021/jp063821k CCC: $33.50
Published on Web 10/04/2006

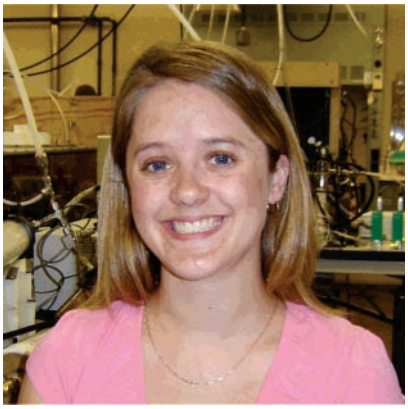

Elizabeth R. Gibson received her undergraduate degree in Chemistry in 2002 from Coe College where she graduated Magna Cum Laude. She is currently a Ph.D. candidate with Professor Vicki Grassian at the University of Iowa. Her current research focus is on the heterogeneous chemistry of mineral dust aerosol and trace atmospheric gases and the climate implications of these reactions. In 2005, Ms. Gibson was selected as one of 50 graduate students from across the nation to attend the 55th annual meeting of Nobel Laureates held in Lindau, Germany. More recently, Ms. Gibson was awarded a 2006 GCEP Graduate Research Environmental Fellowship from the Department of Energy.

Paula K. Hudson received her B. A. in Environmental Science from the University of California, San Diego in 1995 and her doctorate from the University of Colorado in 2001 under the direction of Professor Maggie Tolbert. From 2001 to 2004, Dr. Hudson worked as a postdoctoral researcher at the National Oceanic and Atmospheric Administration in Boulder, CO, with Dr. Daniel Murphy where she participated in several field campaigns, including CRYSTAL-FACE and ICARTT, focusing on single-particle composition measurements. Currently, she is a postdoctoral research associate in the Center for Global and Regional Environmental Research at the University of Iowa with Professor Vicki Grassian. Her research interests include aerosol research and its applications to climate and atmospheric chemistry.

$$MgCl_2\ (s,aq) + 2HNO_3\ (g) \xrightarrow{\%\,RH} Mg(NO_3)_2\ (s,aq) + 2HCl\ (g) \quad (4)$$

Carbonates such as calcite ($CaCO_3$) and dolomite ($CaMg(CO_3)_2$) are thought to be particularly reactive components of mineral dust aerosol[1,5] and readily react with nitrogen oxides, according to the following:

$$CaCO_3\ (s) + 2HNO_3\ (g) \xrightarrow{\%\,RH} Ca(NO_3)_2\ (s,aq) + CO_2\ (g) + H_2O \quad (5)$$

$$CaMg(CO_3)_2\ (s) + 4HNO_3\ (g) \xrightarrow{\%\,RH} Ca(NO_3)_2\ (s,aq) + Mg(NO_3)_2\ (s,aq) + 2CO_2\ (g) + 2H_2O \quad (6)$$

Vicki H. Grassian received her B. S. degree in Chemistry, 1981, from the State University of New York at Albany. From there, she did her graduate studies at Rensselaer Polytechnic Institute (M. S., 1982) and the University of California-Berkeley (Ph.D., 1987). Following postdoctoral positions, she began her independent academic career at the University of Iowa as an Assistant Professor. Professor Grassian is currently a full professor in the Department of Chemistry and holds appointments in the Departments of Chemical and Biochemical Engineering and Occupational and Environmental Health. At the University of Iowa, she has received a Faculty Scholar Award (1999−2001), a Distinguished Achievement Award (2002), a James Van Allen Natural Sciences Faculty Fellowship (2004), and the Regents Award for Faculty Excellence (2006). Her research interests are in the areas of heterogeneous atmospheric chemistry, climate impact of atmospheric aerosols, environmental molecular surface science, and environmental and health aspects of nanoscience and nanotechnology. She has over 100 peer-reviewed publications and is the editor of two books. In 2003 she received an NSF Creativity Award, and in 2005 she was elected as a Fellow of the American Association for the Advancement of Science.

$$CaCO_3\ (s) + N_2O_5\ (g) \xrightarrow{\%\,RH} Ca(NO_3)_2\ (s,aq) + CO_2\ (g) \quad (7)$$

$$CaMg(CO_3)_2\ (s) + 2N_2O_5\ (g) \xrightarrow{\%\,RH} Ca(NO_3)_2\ (s,aq) + Mg(NO_3)_2\ (s,aq) + 2CO_2\ (g) \quad (8)$$

The conversion of $CaCO_3$ particles to $Ca(NO_3)_2$ has been observed in previous laboratory studies for both pure calcium carbonate and authentic mineral dusts.[16−19] The scanning electron microscopy (SEM) images displayed in Figure 1 capture the transformation seen when solid $CaCO_3$ particles react with nitric acid to form aqueous $Ca(NO_3)_2$ droplets. However, these images do not provide quantitative information about the water content of the droplets. For eq 5, it has been shown that both the rate of reaction and the extent of reaction increase as a function of increasing relative humidity ($f(RH)$) and that at most atmospherically relevant $\%RH$ values the nitrate product forms an aqueous layer.[18,20] Additionally, recent laboratory work has shown that N_2O_5 hydrolysis on mineral dust components (e.g., eqs 6 and 8) is enhanced in the presence of higher relative humidity.[21]

Although it is well known from filter-based measurements that Ca^{2+} and NO_3^- are correlated,[5,22,23] it has only been recently shown with single particle analysis methods that calcium carbonate particles entrained in the atmosphere can be completely converted to calcium nitrate.[24−26] This transformation has been observed in several parts of the world including the Middle East and China.[24−26]

There are several interesting aspects of the reaction of nitrogen oxides with atmospheric particles. First, for mineral dust aerosol components such as carbonate, the nitrate salt product has very different physicochemical properties than the carbonate mineral. The nitrate salt aerosol that forms is more hygroscopic and has properties (size, water content, and optical scattering) that can

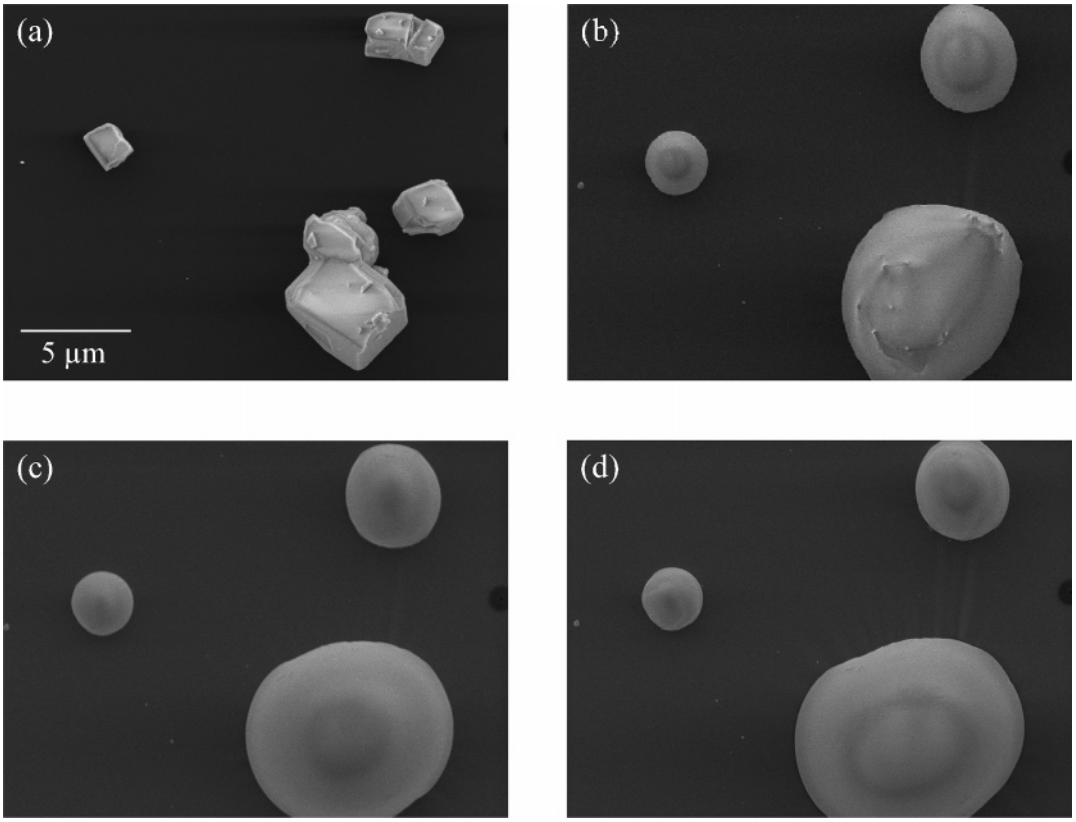

Figure 1. Scanning electron microscopy images of $CaCO_3$ particles (a) before and after (b) 1 h, (c) 2 h, and (d) 4 h of exposure to 20 μTorr of HNO_3 at 41% *RH*. (Adapted from Krueger, B. J.; Grassian, V. H.; Laskin, A.; Cowin, J. P. The transformation of solid atmospheric particles into liquid droplets through heterogeneous chemistry: laboratory insights into the processing of calcium containing mineral dust aerosol in the troposphere. *Geophys. Res. Lett. 30,* 3, doi 10.1029/2002GL106563, Copyright 2003 American Geophysical Union.)

change considerably as a *f*(*RH*).[27] Because both direct (scattering and absorption of solar radiation by particles) and indirect (cloud nucleation activity) climate forcing depend on these properties,[28,29] the climate forcing of the carbonate component of mineral dust aerosol will be significantly altered as the aerosol is transported, reacted, and aged in the atmosphere. Although it is generally recognized that the properties and thus the climate impact of mineral dust aerosol can change as it is transported in the atmosphere,[30,31] there is little quantitative data available on the link between mineral dust aerosol chemistry and climate. Second, nitrate ions are an important chromophore in natural waters and play a crucial role in the chemistry of snowpacks acting as a source of NO_x and OH radicals.[32,33] Photolysis of aqueous nitrate at $\lambda > 290$ nm and pH < 6 proceeds via two major channels:[34−40]

$$NO_3^- + H^+ \xrightarrow{h\nu} NO_2 + OH \quad (9)$$

$$NO_3^- \xrightarrow{h\nu} NO_2^- + O(^3P) \quad (10)$$

The nitrite ion formed in eq 10 can then undergo further photodissociation

$$NO_2^- + H^+ \xrightarrow{h\nu} NO + OH \quad (11)$$

The flux of NO_x from snow and oxidation of organic contaminants in snow and ice by OH radicals formed in eqs 9 and 11 may play a significant role in the chemistry of the atmospheric boundary layer.[32−34,36−38,40−45] Although there have been many studies examining nitrate ion photolysis in snowpacks and natural waters, as discussed above, there has been little consideration of nitrate photochemistry in aqueous atmospheric aerosols.

In this Feature Article, we have focused on the physicochemical properties of several atmospherically relevant nitrate aerosols [$NaNO_3$, $Ca(NO_3)_2$, $Mg(NO_3)_2$, and a 1:1 molar mixture of $Ca(NO_3)_2$ and $Mg(NO_3)_2$] using a newly constructed Multi-Analysis Aerosol Reactor System (MAARS). These measurements include size-selected tandem DMA hygroscopicity analysis, FTIR extinction measurements, and cloud condensation nuclei (CCN) activity. Analysis of these data provides information about the water content of these particles, particle scattering, and the local molecular and electronic environment of the nitrate ions at different relative humidity, and examines how these properties change as a function of *RH*. In addition, we have shown that the increased hygroscopicity of calcium nitrate relative to calcium carbonate results in a significant increase in cloud condensation nuclei activity, thus demonstrating how indirect climate forcing of the atmospherically aged carbonate component of mineral dust is quite different than that of the original aerosol. In a future publication, the UV/vis absorption properties and photochemical reactivity of nitrate aerosols will be discussed in more detail.

Experimental Methods and Data Analyses

Aerosol Measurements of Hygroscopicity, Cloud Condensation Nuclei Activity, and FTIR Extinction. At the University of Iowa, a Multi-Analysis Aerosol flow Reactor System (MAARS) has been recently designed and constructed to measure heterogeneous chemistry, phase transitions, cloud condensation nuclei activity, and infrared extinction of aerosols. The schematic diagram shown in Figure 2 depicts the main components of MAARS.

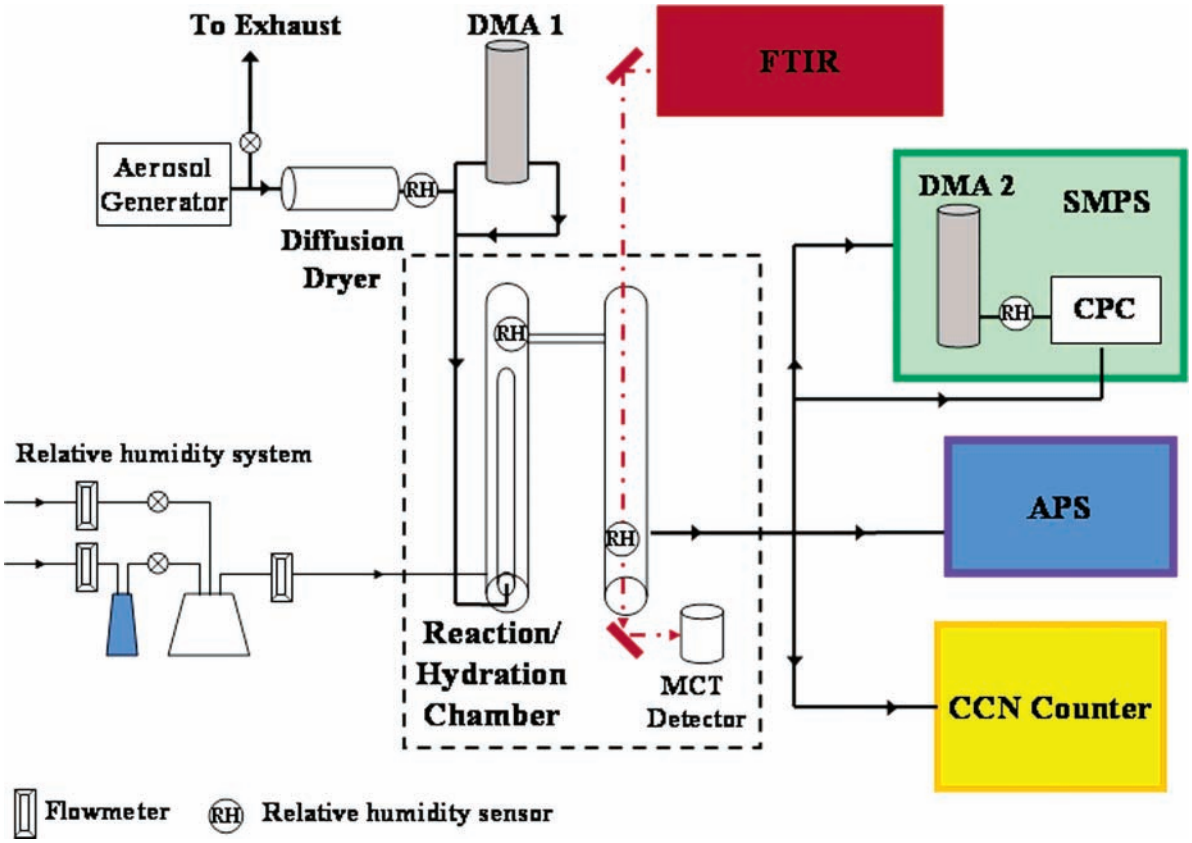

Figure 2. Schematic diagram of the multi-analysis aerosol reactor system (MAARS). MAARS is equipped with multiple tools to measure the properties of aerosols, including a differential mobility analyzer (DMA-1) for size selection; a scanning mobility particle sizer (SMPS), which consists of a second DMA (DMA-2) and a condensation particle counter (CPC), and an aerodynamic particle sizer (APS) for measuring aerosol size distributions; a continuous flow streamwise thermal-gradient cloud condensation nuclei (CCN) counter for determining CCN activity; and an FTIR spectrometer to measure extinction spectra as a *f*(*RH*). The relative humidity is monitored throughout the system with multiple *RH* sensors.

The instrument is equipped with several different aerosol generators including a conventional atomizer, a fluidized bed aerosol generator, and an electrospray atomizer. For the study reported herein, the aerosol is generated with the conventional constant output atomizer (TSI, Inc. Model 3076) from an aqueous salt solution or a suspension of an insoluble powder in water. Once the aerosol is generated, a fraction of the aerosol flows into a diffusion dryer (TSI, Inc. Model 3062) where it is dried to an $RH \leq 10\%$, while the remaining aerosol is sent to the exhaust system. The relative humidity is monitored after the diffusion dryer with an *RH* sensor (Honeywell, HIH-3602-L). Once dried, the aerosol can follow one of two flow streams. Particles are either size-selected with a differential mobility analyzer (DMA-1; TSI, Inc. electrostatic classifier Model 3080) or the full distribution of particles is sent directly into a flow reactor/hydration chamber.

For size-selected particle studies, the monodisperse aerosol flow is directed from the outlet of DMA-1 through the flow reactor/hydration chamber where it can be exposed to reactive gases and/or equilibrated at different *RH* values. For reactive gas exposure studies, a movable injector can be used to control the exposure time of the aerosol with the gas. The relative humidity is controlled using a humidified air stream (flow rate ~4 L/min) that can be adjusted by varying the ratio of wet and dry air supplied by a commercial dry air generator (Parker Balston, Model 75-62). Multiple *RH* sensors are used to monitor the *RH* within ±1% throughout the reaction/hydration chamber. Relative humidity ranging from 3 to 90% is used in size-selected experiments, whereas in experiments measuring full size distributions a maximum of 65% *RH* is reached. The dried aerosol and humidified air are combined in the conditioning chamber of the flow reactor/hydration system. From there, the aerosol flows into the IR cell, which is positioned along the path of the IR beam from a Thermo Nicolet spectrometer (Nexus Model 670) equipped with an MCT-A detector. For size-selected particle experiments, the IR cell is used as an additional conditioning chamber. The *RH* is kept constant throughout the flow reactor/hydration chamber and FTIR cell. In FTIR extinction experiments, full size distributions are required. For these experiments, the aerosol flow bypasses DMA-1 and the infrared cell is used to measure the infrared extinction spectra in the 800 to 7000 cm^{-1} spectral range by co-adding 256 scans at an instrument resolution of 8 cm^{-1}.

Upon exiting the flow reactor/hydration chamber, the aerosol flow can be directed to either a scanning mobility particle sizer (SMPS; TSI, Inc. Model 3936), an aerodynamic particle sizer (APS; TSI, Inc. Model 3321), or a continuous flow streamwise thermal-gradient cloud condensation nuclei (CCN) counter (Droplet Measurement Technologies, Model CCN-2).[46] Particle size distributions are measured by an SMPS, which consists of a second DMA (DMA-2; TSI, Inc. electrostatic classifier Model 3080) and a condensation particle counter (CPC; TSI, Inc. Model 3025A). Sheath air for DMA-2 is provided by a separate external humidification system, maintaining a consistent *RH* throughout the measurement period. In cases where particles larger than 800 nm are generated, an APS is used in addition to the SMPS to measure the complete aerosol size distribution.

For CCN measurements, after the IR extinction cell a portion of the aerosol flow is directed into the CCN counter while the rest is sent directly to the CPC, bypassing DMA-2. In CCN measurements, the number of particles that act as CCN (#CCN) relative to the total number of particles (#CN) counted by the

CPC at a given supersaturation is determined. For the current study, the CCN counter is calibrated to the Köhler curve using ammonium sulfate.[47] The critical supersaturation of an aerosol is defined as the supersaturation value where 50% of the monodisperse aerosol is activated, that is, are able to nucleate a cloud. The maximum fraction of activated particles that can be measured in our system is approximately 0.9. This is largely due to counting inefficiencies in the CPC and CCN counter. Therefore, for the purposes of this study 90% activation is equivalent to 100% activation.

Theoretical Analysis of Hygroscopic Growth Curves and Water Content. Hygroscopic growth curves were obtained by measuring the change in particle diameter with increasing relative humidity. At each *RH* value, the total hygroscopic growth is expressed as the growth factor, $g(RH)$, defined in eq 12 as the ratio of the particle diameter (D_p) after humidification to the volume equivalent diameter (D_0) of the solid particle.

$$g(RH) = \frac{D_p}{D_0} \tag{12}$$

The growth of aqueous solution droplets in humid air can be described by Köhler theory.[48−50] At equilibrium, the *RH* is the ratio of the vapor pressure over a solution droplet to the saturation vapor pressure of water. The relationship between droplet diameter and *RH* at equilibrium is given by eq 13[50]

$$\%\ RH = 100 * a_w S_{Kelvin} = 100 * a_w \exp\left(\frac{4M_w\sigma_{sol}}{RT\rho_w D_p}\right) \tag{13}$$

where a_w is the water activity, S_{Kelvin} is the Kelvin correction factor, M_w is the molar mass of water (kg/mol), σ_{sol} is the surface tension of the solution (N/m), ρ_w is the density of water (kg/m^3), R is the ideal gas constant (J/mol·K), and T is the temperature (K). There are two important effects that determine the vapor pressure over a solution droplet. First, the Kelvin effect, which appears in eq 13 as S_{Kelvin}, describes the increase in vapor pressure over a curved surface relative to a flat surface. Second, dissolved ions or molecules lead to a decrease in vapor pressure over a solution when compared to pure water. The equilibrium vapor pressure will thus depend on solute concentration, species, and temperature and is represented in eq 13 by the activity, a_w.

A theoretical growth curve can be calculated from the solution concentration (c_{sol}) in mass percent, solution density (ρ_{sol}), and solute density (ρ_s), through eq 14,[50]

$$g(RH) = \frac{D_p}{D_0} = \left(\frac{\rho_s}{\frac{c_{sol}}{100}\rho_{sol}}\right)^{1/3} \tag{14}$$

Together, eqs 13 and 14 can be used to calculate a theoretical growth curve. To calculate theoretical growth curves, concentration- and temperature-dependent values of the solution density, surface tension, and water activity are required. Methods for determining these parameters for each of the salts under investigation in this study are described in the Appendix. As discussed in more detail in the Results section, nitrate salt aerosols do not completely dry after atomization. Therefore, D_0 is determined by dividing the droplet diameter measured by the theoretical growth factor at minimal *RH*.

The water content can also be determined from the size-selected aerosol experiments and Köhler theory. To analyze the water content of the nitrate aerosols, we recalculated the Köhler growth curve based on the true values of D_0 determined previously for each salt. Assuming a sphere, the measured peak diameter from the SMPS at a given *RH* value can be used to calculate the volume of the solution droplet. The volume of the droplet at each relative humidity will have a specific solution density that can be matched from the calculated theoretical growth curve. Together, the volume and density can be used to calculate the total mass of the droplet. The mass of the solute present in each solution droplet is assumed to be equivalent to that of a dry particle (with a diameter equivalent to D_0) and can be subtracted from the total droplet mass to yield the mass of water in the aerosol. A ratio of the moles of H_2O to the moles of solute yields the water-to-solute ratio (WSR). Similarly, the mass of the water and solute can be ratioed to determine the WSR on a mass basis. Additionally, the water content of the nitrate aerosols can be compared to each other on a per nitrate basis by calculating a water-to-nitrate ion ratio (WNR). This analysis is also done using the theoretical growth curve and taking into consideration the number of nitrate ions present in the molecular formula of each salt.

FTIR Absorption Band Curve Fitting. Infrared extinction spectra reported here were analyzed using the peak fitting module in OriginPro 7.5. The absorption bands present in the spectral region extending from 900 to 2000 cm^{-1} were fit to Gaussians, corresponding to the observed nitrate and water absorbance bands, to obtain exact peak positions, full-width at half-maxima (fwhm) values, and peak areas. The maximum error in the peak position determined from each fit is ±10 cm^{-1}. The results of the curve-fitting analysis are presented in the Discussion section.

Sources of Chemicals and Materials. All of the salts under investigation in this work are commercially available and were used as received. Ammonium sulfate (ACS) was purchased from Fisher Scientific; $NaNO_3$ (ACS) from Sigma-Aldrich, ACS; $Ca(NO_3)_2$ (ACS, 99.0−103.0%) and $Mg(NO_3)_2$ (ACS, 98.0−102.0%) from Alfa Aesar. Ammonium sulfate and nitrate aerosols are generated from either a 1 or 5 wt % by volume (wt %) aqueous solution of the salt. $CaCO_3$ powder (OMYA) was also used as received and atomized from a suspension of the insoluble powder in water. In hygroscopic growth and CCN measurements, particles with mobility diameters of ca. 100 nm are size-selected from a 1 wt % solution. FTIR extinction measurements required the use of a more concentrated aerosol solution (5 wt %) and the full aerosol distribution in order to generate enough signal to obtain a measurable spectrum.

Results

Hygroscopic Growth of 100 nm Ammonium Sulfate: A Test System. The hygroscopic properties of ammonium sulfate are well understood and have been characterized using several different techniques[50−55] making it an ideal system to test the apparatus MAARS described here. Figure 3a displays a series of Gaussian fits to the measured SMPS size distributions of size-selected $(NH_4)_2SO_4$ as a function of *RH*. The fits have been normalized to the peak concentration. There is no shift in diameter until the deliquescence *RH* is reached, at which point there is a distinct and abrupt increase in size of the particles as the particles undergo a solid to liquid phase transition. Figure 3b displays the measured growth factor and the measured deliquescence, which occurs at 80 ± 1% *RH*, in excellent agreement with values reported previously.[50,51,53]

Hygroscopic Growth of 100 nm Size-Selected Sodium Nitrate Aerosol. The hygroscopic properties of $NaNO_3$ have been examined previously with several different techniques.[50,52,56−58] $NaNO_3$ is expected to deliquesce at 74.5% *RH*

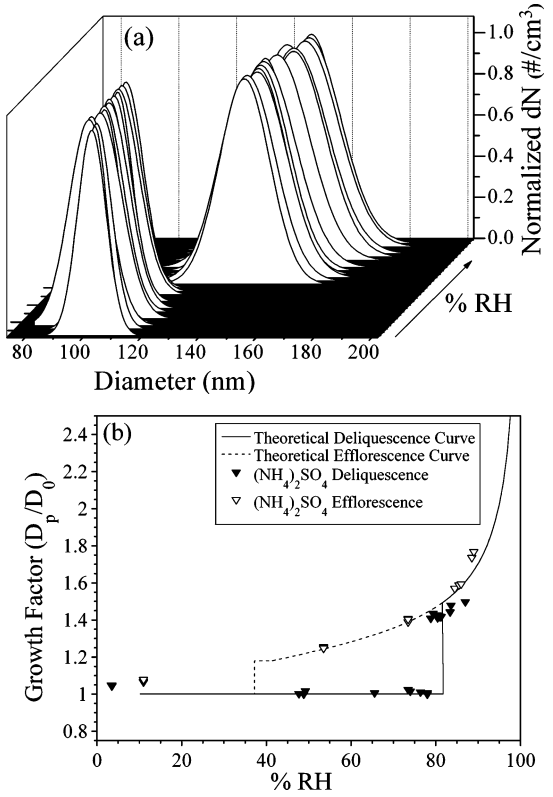

Figure 3. (a) Hygroscopic growth and measured phase transition of 100 nm $(NH_4)_2SO_4$. The distributions displayed are Gaussian fits to the size-selected SMPS distributions, normalized to the peak concentration. (b) Measured growth factor for 100 nm $(NH_4)_2SO_4$ as a function of increasing (▼) and decreasing (▽) *RH*. The solid and dashed lines represent the theoretical deliquescence and efflorescence, respectively, of $(NH_4)_2SO_4$ as calculated from Köhler theory.

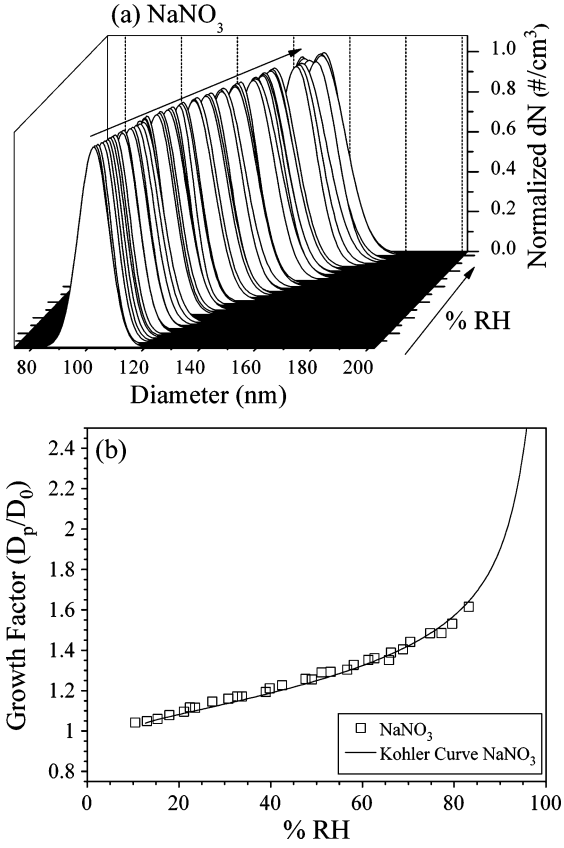

Figure 4. (a) Hygroscopic growth and (b) measured growth factor of $NaNO_3$ size-selected at 100 nm as a function of *RH*. In (a), the distributions displayed are Gaussian fits to size-selected SMPS distributions from a representative data set. Each distribution has been normalized to the peak concentration. In (b), each data point is the average of 2−6 measurements. The error associated with each data point is the standard deviation of these multiple measurements and is on the order of the size of the symbols.

and its efflorescence point, liquid to solid transition, has been measured between 35 and 0.05% *RH*.[52] The hygroscopic behavior of 100 nm $NaNO_3$ is displayed in Figure 4a. The peak diameter of the aerosol increases continuously from 100 nm at 10% *RH* to 158 nm at 83% *RH*. These data show that unlike ammonium sulfate, $NaNO_3$ does not completely dry out even at 10% *RH*. This is consistent with the low efflorescence *RH* reported, and continual growth of the particles is observed. Thus, the $NaNO_3$ aerosol particles are present as solution droplets throughout the entire measurement as reflected in the experimental growth curve, shown in Figure 4b. Because the $NaNO_3$ particles are already solution droplets before size selection in DMA-1, D_0 is not equivalent to 100 nm and must be calculated from the Köhler growth curve. For $NaNO_3$, D_0 has a value of 98 nm based on the theoretical $g(RH)$ at 15% *RH*. This calculated D_0 is then used in eq 12 to yield an experimental growth curve. The growth factor for $NaNO_3$ increases from 1.04 ± 0.02 at 10% *RH* to 1.62 ± 0.01 at 83% *RH*; this too is in good agreement with previous literature.[50]

Hygroscopic Growth and CCN Activity of 100 nm Size-Selected Calcium Nitrate Aerosol: Comparison to 100 nm Size-Selected $CaCO_3$. In this section, the growth curve of $Ca(NO_3)_2$ is presented and also compared to $CaCO_3$. As discussed in the Introduction, $CaCO_3$ can be converted to $Ca(NO_3)_2$ upon reaction with nitrogen oxides in the atmosphere. Thus, the differences in the physicochemical properties of these two aerosol types have important atmospheric implications. Figure 5 displays the growth of 100 nm $CaCO_3$ and $Ca(NO_3)_2$. For $CaCO_3$, no change in peak diameter is observed as a $f(RH)$, while $Ca(NO_3)_2$ grows significantly to 160 nm at higher *RH* values. Values of $g(RH)$ can be calculated for each aerosol, and these are plotted in Figure 6. As noted, there is no observable growth of $CaCO_3$ particles up to 85% *RH*, and $g(RH)$ has an average value of 1.00 ± 0.02 over the entire relative humidity range. It has been shown by previous FTIR and thermogravimetric analysis measurements of water adsorption on $CaCO_3$ that 1−3 monolayers of water can be formed on the carbonate surface with increasing *RH*.[59,60] If it is assumed that three monolayers is equivalent to between 0.5 and 1 nm at most, then this would correspond to a growth factor near 1.01, in good agreement with our results.

In comparison, the measured growth factor of size-selected 100 nm $Ca(NO_3)_2$ particles (shown in Figure 6) is quite different. $Ca(NO_3)_2$ particles formed from saturated solution droplets are amorphous hydrates; that is, they are never truly "dry".[61] As a result, $g(RH)$ will never be unity and the true value of D_0 must be determined from the theoretical growth curve. For $Ca(NO_3)_2$, the experimental data has been matched to the theoretical growth curve at 15% *RH* yielding a calculated D_0 of 89 nm. The deliquescence transition observed near 10% *RH* corresponds to the amorphous hydrate and not anhydrous $Ca(NO_3)_2$. Because amorphous $Ca(NO_3)_2$ deliquesces at 10% *RH*, it exists as an aqueous droplet at atmospherically relevant *RH*. With a growth factor of 1.13 ± 0.01 at 10% *RH* and 1.77 ± 0.05 at 85% *RH*, $Ca(NO_3)_2$ nearly doubles in diameter, corresponding to an 8-fold increase in volume, at the highest *RH* value.

On the basis of the hygroscopic nature of $Ca(NO_3)_2$, it is expected that the cloud nucleation activity of $Ca(NO_3)_2$ will be quite high and that $Ca(NO_3)_2$ will have much greater activity

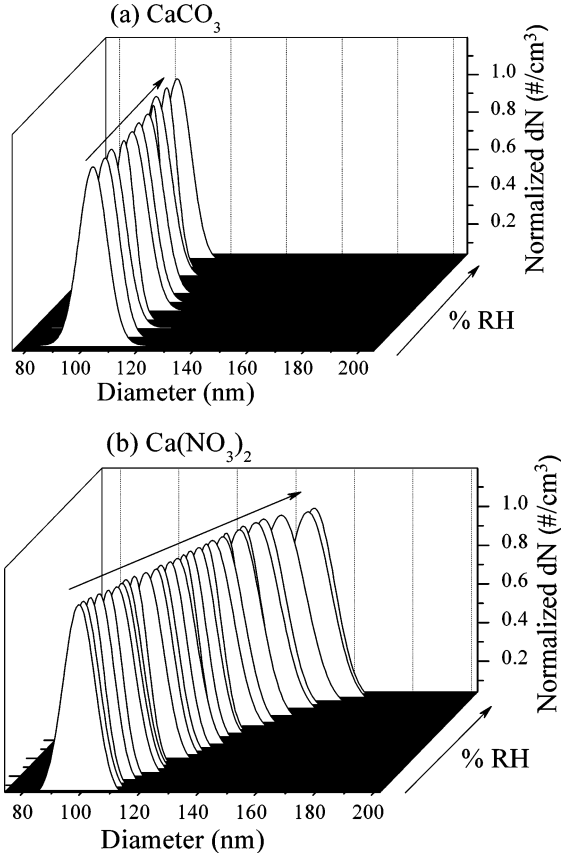

Figure 5. Hygroscopic growth of 100 nm size-selected (a) $CaCO_3$ and (b) $Ca(NO_3)_2$ as a function of relative humidity. The $CaCO_3$ and $Ca(NO_3)_2$ distributions displayed are Gaussian fits to the size-selected SMPS distributions from a representative data set, normalized to the peak concentration. In (a), there is no observable change in particle diameter. In (b), the particles increase in peak diameter by nearly 60%, from 100 nm at 4% *RH* to 160 nm at 85% *RH*.

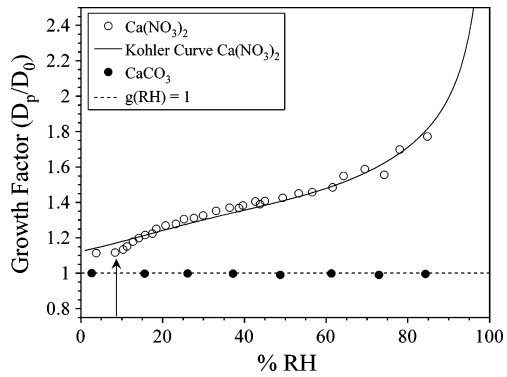

Figure 6. Measured growth factors for size-selected 100 nm $CaCO_3$ (filled circles) and $Ca(NO_3)_2$ (open circles) as a $f(RH)$. The dashed line represents a growth factor equivalent to one. The measured growth factor for $Ca(NO_3)_2$ is based on a dry diameter of 89 nm. The phase transition from an amorphous $Ca(NO_3)_2$ particle to an aqueous droplet is indicated by the arrow.

than $CaCO_3$. The CCN activity of 100 nm $CaCO_3$ and $Ca(NO_3)_2$ aerosol particles were measured and compared. These data are shown in Figure 7 as a function of water supersaturation above 100% *RH* (% SS). In Figure 7, 0.1% supersaturation corresponds to 100.1% *RH* and the dashed line represents the 50% activation point. The critical supersaturation for $Ca(NO_3)_2$ is 0.11 ± 0.01% SS, the same as that found for $(NH_4)_2SO_4$, which represents a large component of CCN in the atmosphere.[62,63] In contrast, at 0.11% SS none of the $CaCO_3$ aerosol is activated. The difference between the CCN activity of the different aerosols is further

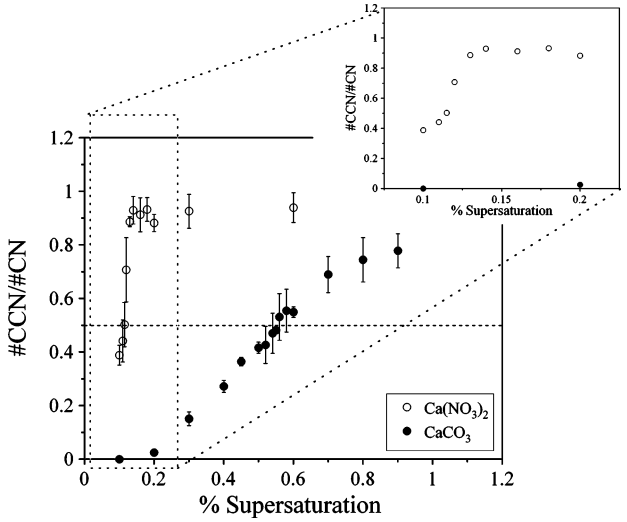

Figure 7. CCN activity for 100 nm size-selected $Ca(NO_3)_2$ (open circles) and $CaCO_3$ (filled circles). The data are plotted as the fraction of particles that can nucleate a cloud (#CCN/#CN) as a function of percent water supersaturation (% SS) above 100% *RH*. An expanded view of the region from 0.075 to 0.225% SS is shown in the inset, where the differences between $CaCO_3$ and $Ca(NO_3)_2$ are greatest. Integration of this region shows that the CCN ability of $Ca(NO_3)_2$ is nearly 2 orders of magnitude greater than that of $CaCO_3$. The dashed line indicates the critical supersaturation where 50% of the particles can activate a cloud.

illustrated at 0.2% SS, shown in the inset of Figure 7, where $Ca(NO_3)_2$ is essentially 100% activated and $CaCO_3$ is less than 2% activated. Thus, from these results, it can be concluded that as $CaCO_3$ undergoes processing by HNO_3 and N_2O_5 in the troposphere to form $Ca(NO_3)_2$, its ability to nucleate clouds increases significantly and is nearly 2 orders of magnitude greater than the freshly emitted carbonate aerosol between 0.075 and 0.2% SS. It should be noted that because 100 nm $Ca(NO_3)_2$ aerosol particles are not completely dry when size-selected, the true dry diameter of the particles is 89 nm, as discussed previously. Therefore, the percent SS result presented here represents an upper limit for $Ca(NO_3)_2$ because 100 nm particles would be expected to become active even at *lower* percent SS.

Hygroscopic Growth of Other Nitrate Aerosols: 100 nm Size-Selected Magnesium Nitrate and 1:1 Calcium/Magnesium Nitrate Aerosol. Other atmospherically relevant nitrate aerosols, formed via reaction with nitrogen oxides (e.g., eqs 4, 6, and 8) were also investigated. Figure 8 illustrates the growth of size-selected 100 nm $Mg(NO_3)_2$ and 100 nm particles from a 1:1 molar mixture of $Ca(NO_3)_2$ and $Mg(NO_3)_2$. For $Mg(NO_3)_2$, continual growth is observed from 100 nm near 10% *RH* to 148 nm at 83% *RH*. The 1:1 calcium/magnesium nitrate mixture also displays continual growth, increasing in diameter by nearly 50 nm at higher *RH*. $Mg(NO_3)_2$ and the mixture show size-selected distributions with peak diameters less than 100 nm at $RH <$ 10%. This is due to further drying of the aerosol particles after they have been size-selected and are exposed to *RH* in the flow reactor/hydration chamber lower than that of the diffusion dryer.

Theoretical and measured growth curves for this salt and salt mixture are shown in Figure 9. Like $NaNO_3$ and $Ca(NO_3)_2$, both $Mg(NO_3)_2$ and the 1:1 mixture do not completely recrystallize after drying and are present as aqueous solution droplets throughout the experiment. D_0 is calculated to be 77 and 85 nm for $Mg(NO_3)_2$ and 1:1 $Ca(NO_3)_2 + Mg(NO_3)_2$, respectively (calculated from the theoretical $g(RH)$ at 15% *RH* for $Mg(NO_3)_2$ and 21% *RH* for the mixture). On the basis of these calculated dry diameters, measured values of $g(RH)$ are 1.34 ± 0.01 at 10% *RH* and 1.94 ± 0.02 at 83% *RH* for $Mg(NO_3)_2$ and 1.23

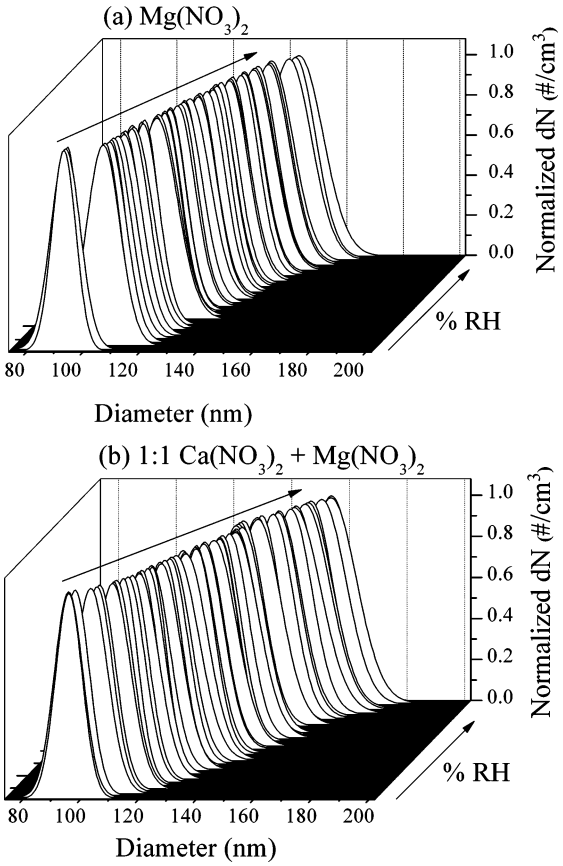

Figure 8. Hygroscopic growth of 100 nm size-selected (a) $Mg(NO_3)_2$ and (b) 1:1 $Ca(NO_3)_2 + Mg(NO_3)_2$ as a function of relative humidity. The representative data set displayed for each salt shows Gaussian fits to the size-selected SMPS distributions. Each size distribution has been normalized to the peak concentration.

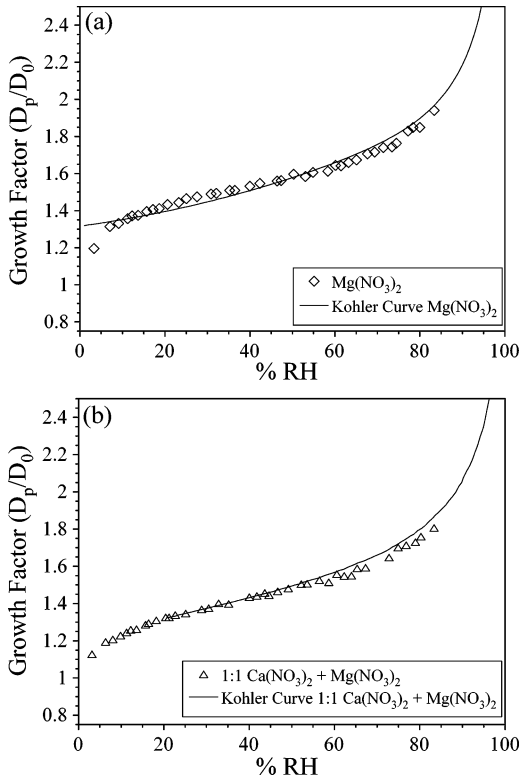

Figure 9. Measured $g(RH)$ of 100 nm size-selected (a) $Mg(NO_3)_2$ and (b) 1:1 $Ca(NO_3)_2 + Mg(NO_3)_2$ as a $f(RH)$. The measured growth factor for $Mg(NO_3)_2$ and 1:1 $Ca(NO_3)_2 + Mg(NO_3)_2$ are based on dry diameters of 77 and 85 nm, respectively.

$\pm$ 0.01 at 10% *RH* and 1.81 $\pm$ 0.01 at 83% *RH* for the mixture. It should be noted that even though the calculated values of D_0 are less than 100 nm, the change in the theoretical growth curve due to the Kelvin effect is less than 1%.

FTIR Extinction Spectra of Nitrate Salt Aerosols from 10 to 65% *RH*. Infrared extinction data can be used to further characterize the water content of the particles and changes in light scattering, both as a function of *RH*. As noted previously, FTIR experiments are performed with 5 wt % solutions of $NaNO_3$, $Ca(NO_3)_2$, $Mg(NO_3)_2$, and the 1:1 $Ca(NO_3)_2 + Mg(NO_3)_2$ mixture and are of the full size distributions. However, FTIR extinction measurements can lend additional information and support to the size-selected hygroscopic growth and CCN results discussed already.

Figure 10 displays IR extinction spectra for $NaNO_3$, $Ca(NO_3)_2$, $Mg(NO_3)_2$, and the 1:1 $Ca(NO_3)_2 + Mg(NO_3)_2$ mixture from 800 to 7000 cm^{-1}. The presence of absorbance peaks in the O−H stretching ($\nu(H_2O)$) near 3400 cm^{-1} and bending regions ($\delta(H_2O)$) near 1640 cm^{-1} for each nitrate at both low and high *RH* is indicative of water associated with the nitrate particles. The magnitude of the intensity of the $\nu(H_2O)$ absorbance band varies depending on the nitrate salt. At lower *RH*, $NaNO_3$ has a minimal $\nu(H_2O)$ peak, whereas the 1:1 mixture has the most water associated with the particles. As relative humidity increases, the $\nu(H_2O)$ peak red shifts between 12 and 62 cm^{-1} for all of the nitrate salts. The $\delta(H_2O)$ absorbance band broadens and shifts by 5−10 cm^{-1} as a $f(RH)$ for each of the salts as well. In addition, the growth of the O−H stretching and bending regions indicates that the aerosol particles are taking up more water as *RH* increases, supporting the results obtained in the hygroscopic growth measurements discussed previously. For the divalent nitrate salts it can also be concluded that crystalline hydrates do not form, as the crystalline forms give rise to a more structured O−H band in the stretching region and a sharper O−H band in the bending region.[64] In comparison, the more poorly defined broad absorbance band observed is characteristic of an amorphous hydrate solid or aqueous aerosol.[64]

Besides the increase in the integrated absorbance of the water stretching and bending as a function of increasing *RH*, there is also a visible increase in the amount of light scattering by the aerosol particles at wavelengths above 4000 cm^{-1}. The amount of scattered light above 4000 cm^{-1} increases by nearly a factor of 3 at higher *RH*. This result is consistent with the increase in size of the aerosol particles at the higher relative humidity.

Changes in the size distribution can be seen in the representative full size distributions shown in Figure 11 for each nitrate salt aerosol at low and high relative humidity. There is a noticeable increase in the peak diameter of the distribution providing further evidence that the aerosol particles are taking up water and growing in size. Although exact growth factors are difficult to obtain from the full distribution data, general comparisons to results from size-selected experiments can be made. The peak diameter of the distribution increases by a factor of 1.26, 1.13, 1.23, and 1.23 for $NaNO_3$, $Ca(NO_3)_2$, $Mg(NO_3)_2$, and 1:1 $Ca(NO_3)_2 + Mg(NO_3)_2$, respectively. A ratio of the $g(RH)$ at 60% *RH* to the $g(RH)$ at 15% *RH* from size-selected measurements, similar to the *RH* measured in extinction experiments, compares favorably to the increase in the peak diameter of the full distributions for each of the nitrate salts.

As relative humidity increases, there are also changes in the nitrate absorption bands. For clarity, the region extending from 800 to 1600 cm^{-1} is shown in Figure 12. The observed frequencies for the nitrate vibrational modes seen in this spectral

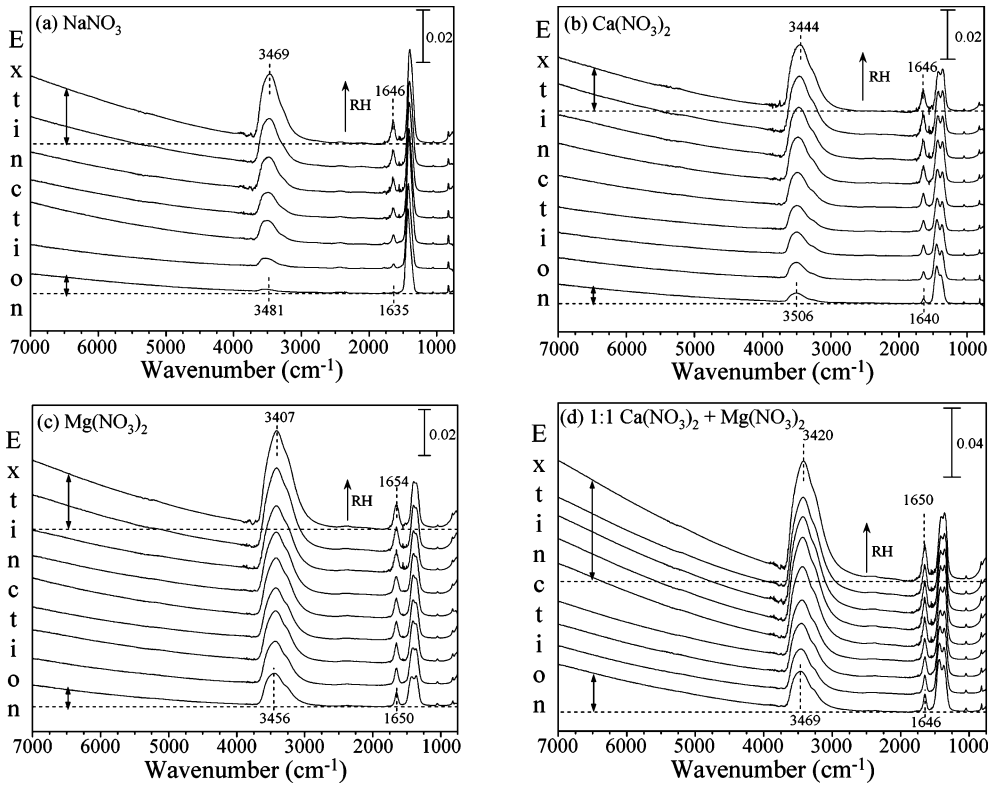

Figure 10. IR extinction spectra of (a) $NaNO_3$, (b) $Ca(NO_3)_2$, (c) $Mg(NO_3)_2$, and (d) 1:1 $Ca(NO_3)_2 + Mg(NO_3)_2$ in the 800−7000 cm^{-1} spectral range. The spectra were recorded as a *f*(*RH*), increasing along the *y* axis; (a) 6, 15, 24, 32, 41, 52, and 62% *RH*; (b) 8, 14, 20, 27, 33, 42, 49, 56, and 63% *RH*; (c) 8, 15, 21, 27, 35, 42, 48, 56, and 65% *RH*; (d) 9, 13, 22, 30, 38, 45, 48, 52, and 61% *RH*. In each set of spectra, absorptions due to the O−H stretching (3000−3800 cm^{-1}) and bending (approximately 1645 cm^{-1}) modes of water are observed. Absorptions due to nitrate ion are seen near 830 and 1050 cm^{-1} and as a doublet between 1350 and 1450 cm^{-1}. See Table 1 for specific assignments.

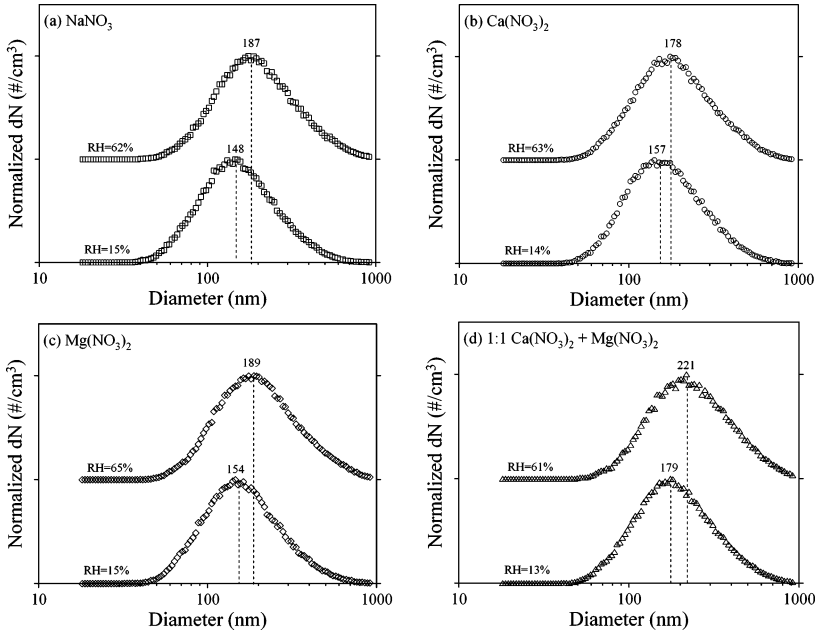

Figure 11. Representative full size distributions at low and high relative humidity for (a) $NaNO_3$, (b) $Ca(NO_3)_2$, (c) $Mg(NO_3)_2$, and (d) 1:1 $Ca(NO_3)_2 + Mg(NO_3)_2$. Each distribution has been normalized to peak concentration. The distribution measured at higher *RH* has been offset for clarity. The position of the peak diameter in each distribution is given.

region for each of the salts are given in Table 1. As described previously, the nitrate absorptions have been curve fit in order to determine frequency shifts as a *f*(*RH*). Figure 12a shows that in the nitrate region of the $NaNO_3$ spectra the $\nu_3(NO_3^-)$ band appears as an asymmetric absorption band centered at 1427 cm^{-1}, with a shoulder at 1367 cm^{-1} at low *RH*. The shape of this band is consistent with previous measurements of $NaNO_3$ aerosol.[65] When relative humidity increases, there is a visible shift of the ν_3 band to 1407 cm^{-1}. The shoulder becomes less apparent but is still evident near 1362 cm^{-1}. At *RH* < 10%, the ν_3 nitrate peaks of $Ca(NO_3)_2$ are located at 1452 and 1368 cm^{-1}. When exposed to a higher *RH* of approximately 60%, these peaks shift to 1426 and 1351 cm^{-1}, respectively. The ν_1 symmetric stretch shifts slightly from 1048 to 1046 cm^{-1} as well. For $Mg(NO_3)_2$, the ν_3 doublet has peaks at 1438 and 1356 cm^{-1} at low *RH*, which shift to 1412 and 1350 cm^{-1} at higher

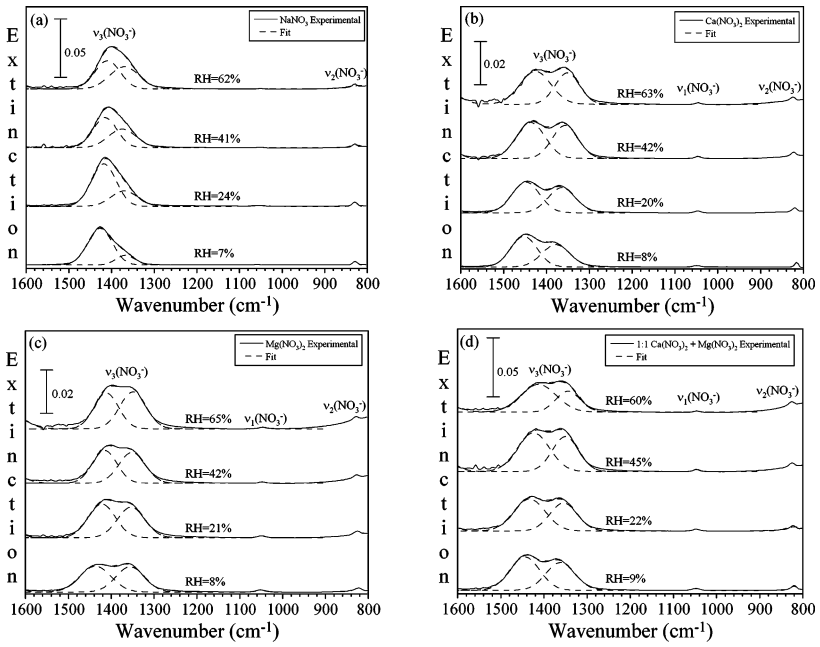

Figure 12. IR spectra in the 800−1600 cm^{-1} range for (a) $NaNO_3$, (b) $Ca(NO_3)_2$, (c) $Mg(NO_3)_2$, and (d) 1:1 $Ca(NO_3)_2 + Mg(NO_3)_2$. The $\nu_1(NO_3^-)$ absorbance bands are each fit to a Gaussian, shown as the dashed lines. The $\nu_3(NO_3^-)$ absorbance band, which appears as a doublet, is fit to two Gaussians.

TABLE 1: Vibrational Mode Assignment for $NaNO_3$, $Ca(NO_3)_2$, $Mg(NO_3)_2$, and 1:1 $Ca(NO_3)_2 + Mg(NO_3)_2$[a]

	observed frequency (cm^{-1})	
vibrational mode assignment	low *RH*[b]	high *RH*[c]
$NaNO_3$		
symmetric stretch, ν_1	1059	1051
out-of-plane deformation, ν_2	830	830
asymmetric stretch, ν_3	1367 (sh),[d] 1427	1362 (sh), 1407
$\Delta\nu_3$[e]	60	45
$Ca(NO_3)_2$		
symmetric stretch, ν_1	1048	1046
out-of-plane deformation, ν_2	816	824
asymmetric stretch, ν_3	1368, 1452	1351, 1426
$\Delta\nu_3$	84	75
$Mg(NO_3)_2$		
symmetric stretch, ν_1	1052	1046
out-of-plane deformation, ν_2	824	828
asymmetric stretch, ν_3	1356, 1438	1350, 1412
$\Delta\nu_3$	82	64
1:1 $Ca(NO_3)_2 + Mg(NO_3)_2$		
symmetric stretch, ν_1	1049	1047
out-of-plane deformation, ν_2	819	825
asymmetric stretch, ν_3	1369, 1450	1345, 1414
$\Delta\nu_3$	81	69

[a] Peak positions are determined from Gaussian fits to the absorption bands in the FTIR spectra. [b] <10% *RH*. [c] >60% *RH*. [d] sh = shoulder. [e] $\Delta\nu_3$ is the difference in the splitting of the ν_3 vibrational mode.

RH. In the mixture, the NO_3^- asymmetric stretch appears as a doublet with peaks at 1450 and 1369 cm^{-1} (low *RH*) and 1414 and 1345 cm^{-1} (high *RH*). The ν_1 symmetric stretch shifts by 6 and 2 cm^{-1} for $Mg(NO_3)_2$ and the 1:1 mixture, respectively. Further discussion of the significance of the changes in the IR extinction spectra are presented in the following section.

Discussion

Aerosol Water-to-Solute Ratio as a *f*(*RH*) for Ammonium Sulfate and Nitrate Salts. The results presented above are discussed here in terms of aerosol water content and its impact for atmospheric processes as well as the local molecular environment of the nitrate anion. The water content depends highly on the phase of the salt. As discussed previously, ammonium sulfate has a deliquescence *RH* (*DRH*) of 80% and is known to effloresce at 37% *RH*. We measure here the deliquescence transition at 80 ± 1% *RH* (see Figure 3b). For $NaNO_3$, no phase transition is observed in this study (see Figure 4b); however, single particle levitation studies have shown that $NaNO_3$ has a *DRH* of 74.5% *RH*, but it effloresces anywhere from 35% *RH* and below.[52] The lack of an observed phase transition is not unexpected because previous work has shown that the conditions in the diffusion dryer are often not at a low enough relative humidity to induce efflorescence.[50]

On the basis of thermodynamic considerations, $Ca(NO_3)_2$ is expected to deliquesce at 11.8% *RH* to form the crystalline tetrahydrate, $Ca(NO_3)_2 \cdot 4H_2O$, which in turn has a *DRH* of 57%.[61,66] In this work, a phase transition is observed at around 10% *RH* for $Ca(NO_3)_2$ (see Figure 6) followed by continual growth of the $Ca(NO_3)_2$ aerosol, indicating that the aerosol formed consists largely of amorphous $Ca(NO_3)_2$. The growth curve and deliquescence point measured in this study is consistent with previous literature results.[20,24,61] As with $Ca(NO_3)_2$, single-particle levitation studies have shown that $Mg(NO_3)_2$ does not effloresce even at low *RH* but may form amorphous particles at $RH \leq 3\%$.[67,68] The continual growth of the aerosol droplets is in good agreement with previous literature.[68,69] The significant increase in $g(RH)$ from 3 to 10% *RH* is potentially due to the deliquescence of amorphous $Mg(NO_3)_2$. Deviation of the measured growth curves for the divalent salts from the theoretical growth predicted by Köhler theory below 50% *RH* may be due to the formation of contact-ion pairs. Zhang et al. have observed that below this point aqueous $Mg(NO_3)_2$ droplets grow linearly, whereas above this point there is an exponential increase in size.[68] A similar trend can be observed in our data (see Figure 9a). Additionally, differences in measured and theoretical values of $g(RH)$ may be due to assumptions made in calculating the theoretical growth curve, such as extrapolation of water activity data discussed in the Appendix, for each of the nitrate salts. The behavior of the 1:1 mixture (Figure 9b) is similar to that of the pure nitrate salt components.

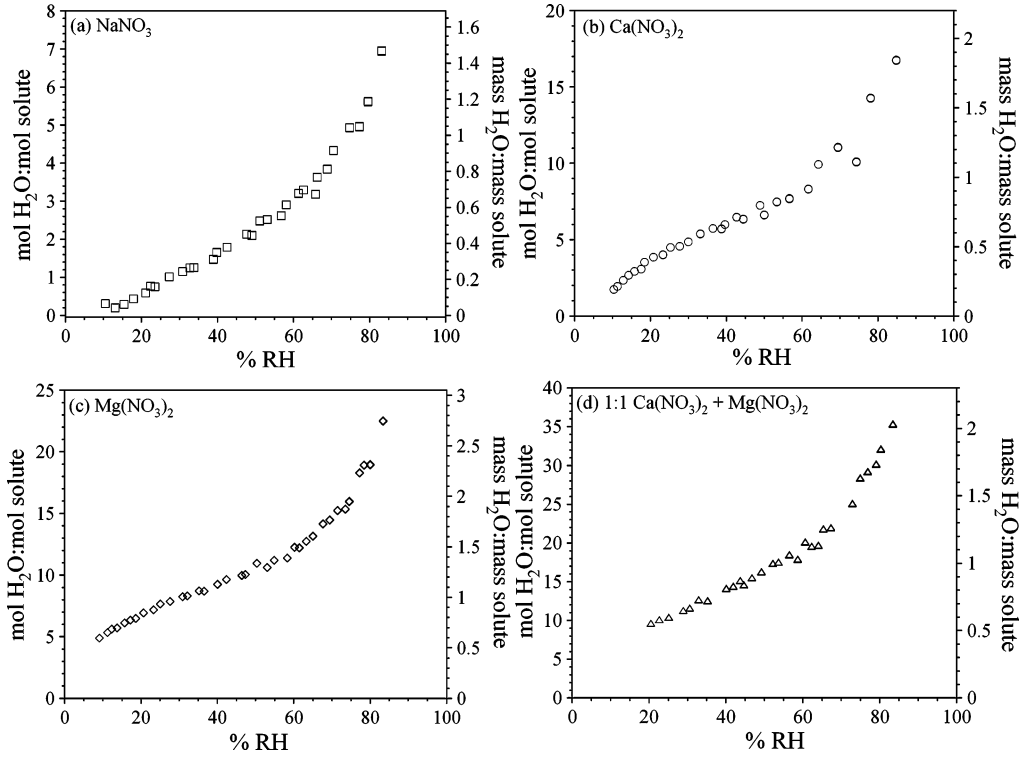

Figure 13. Calculated ratio of H_2O to solute by moles (left axis) and mass (right axis) for (a) $NaNO_3$, (b) $Ca(NO_3)_2$, (c) $Mg(NO_3)_2$, and (d) 1:1 $Ca(NO_3)_2$ + $Mg(NO_3)_2$. The ratios shown correspond to solution molalities (m) ranging from (a) 8−200 m, (b) 3−32 m, (c) 2−11 m, and (d) 1−6 m.

The water content of each nitrate salt can be determined from Köhler theory. The calculated water-to-solute ratio for each nitrate on a molar and mass basis is shown in Figure 13. For $NaNO_3$, the molar WSR increases from 0.31 ± 0.08 at 10% *RH* to 6.94 ± 0.03 at 83% *RH*. These values are equivalent to mass ratios of 0.07 ± 0.02 and 1.47 ± 0.01 at low and high *RH*, respectively. The WSR of $Ca(NO_3)_2$, on a mole and mass basis, calculated in this work and shown in Figure 13b are in excellent agreement with those determined by single particle levitation experiments.[61] At 15 and 70% *RH*, a WSR of 2.94 ± 0.03 and 11.06 ± 0.23 is determined, which corresponds to mass ratios of 0.32 ± 0.003 and 1.21 ± 0.03, respectively. $Mg(NO_3)_2$ and the 1:1 $Ca(NO_3)_2$ + $Mg(NO_3)_2$ mixture have the largest calculated WSR. At 11 and 83% *RH*, the molar WSR for $Mg(NO_3)_2$ is 5.36 ± 0.12 and 22.54 ± 0.90, respectively, or 0.60 ± 0.01 and 2.74 ± 0.11 on a mass basis. The calculated molar WSR for $Mg(NO_3)_2$ (shown in Figure 13c) is in good agreement with values reported previously in single particle levitation studies.[67,70,71] For the mixture, the molar WSR is 9.64 ± 0.08 at 20% *RH* and 35.31 ± 0.16 at 83% *RH* (0.56 ± 0.01 and 2.04 ± 0.01 by mass).

To compare the different salts and salt mixture in terms of the water content for each aerosol at a given *RH* value, we have determined the water-to-nitrate ion ratio from Köhler theory. This ratio is displayed in Figure 14. It can be seen that, when normalized to the nitrate ion, there is quite a bit of variation in the water content. $Mg(NO_3)_2$ has the highest WNR, followed by the mixture, $Ca(NO_3)_2$, and $NaNO_3$ with the lowest WNR. This variation highlights the influence of the metal cation on the amount of water that is taken up by the aerosol. Neglecting the mixture, the WSR and WNR behavior, as determined from size-selected experiments, trends with the hydration energy of the cations where $Mg^{2+} > Ca^{2+} > Na^{+}$.[72]

The WNR can also be calculated from the IR extinction data by integrating the areas of the $\nu(H_2O)$ and $\nu_3(NO_3^-)$ regions of the spectra and assuming that the integrated cross sections ($\bar{\sigma}$) of these two bands are equivalent to that of bulk water and to values previously determined for nitrate.[64,73,74] The IR extinction spectra of the nitrate aerosol full size distributions give WNR values that are a factor of ca. 2 higher than those determined from Köhler theory for the 100 nm size-selected experiments. The differences between the two methods for calculating the water-to-nitrate ion ratio arise from assumptions made in determining $\bar{\sigma}$ (for bulk water and nitrate) and when applying Köhler theory to the size-selected experiments.

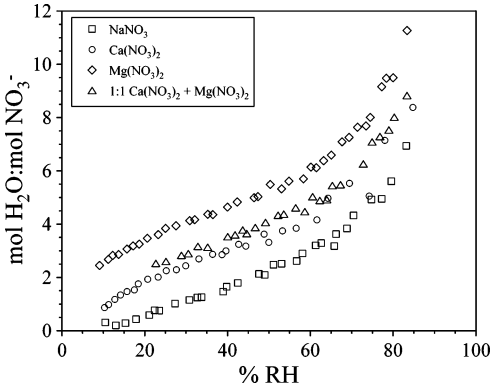

Figure 14. Molar water-to-nitrate ion ratio for $NaNO_3$ (□), $Ca(NO_3)_2$ (○), $Mg(NO_3)_2$ (◇), and 1:1 calcium:magnesium nitrate mixture (△). The water-to-nitrate ion ratio was calculated from the theoretical growth curve for each salt. See the text for further details.

To further understand the significance of the calculated WSR, the water content of the nitrate salts can be compared with the water content found in ammonium sulfate and montmorillonite, another component of mineral dust aerosol.[27,75] Montmorillonite is a swellable clay mineral that can readily take up water in the interlayer sheets of the clay. Below 37% *RH*, the efflorescence point of ammonium sulfate, $(NH_4)_2SO_4$ is a dry particle, whereas $Ca(NO_3)_2$ and $Mg(NO_3)_2$ contain as much as 39 and 50% water

by mass, respectively. The water associated with $Ca(NO_3)_2$ and $Mg(NO_3)_2$ is as much as 8−10 times greater than the water content in montmorillonite, which contains approximately 5% water by mass at similar *RH* value.[75] Between the efflorescence and deliquescence transitions of ammonium sulfate at 37 and 80% *RH*, $(NH_4)_2SO_4$ may contain some amount of water, but only after it has deliquesced at 80% *RH*. Even if $(NH_4)_2SO_4$ has deliquesced, the water content of calcium and magnesium nitrate will still be greater within this range. Near 80% *RH*, the molar WSR of $Ca(NO_3)_2$ and $Mg(NO_3)_2$ measured in this work is greater than that of deliquesced $(NH_4)_2SO_4$ by a factor ranging from 1.5 to 2.0. $NaNO_3$ has a lower molar WSR than deliquesced ammonium sulfate. These results indicate that $Ca(NO_3)_2$ and $Mg(NO_3)_2$, as well as mixtures of these salts, are highly hygroscopic over the full range of atmospherically relevant *RH* and has considerably greater water content for heterogeneous chemistry than $(NH_4)_2SO_4$ and montmorillonite.

***RH* Dependence on the Molecular and Electronic Structure of the Nitrate Ion.** As discussed in the Results section, as the nitrate aerosol particles are exposed to higher *RH* there is a visible change in the infrared spectra of the nitrate ion, indicating that the molecular structure of the nitrate ion is dependent on *RH*. The D_{3h} symmetry of an isolated nitrate ion generates four vibrational frequencies, two of which are doubly degenerate. These bands appear at 1045, 830, 1370, and 723 cm^{-1}, and correspond to the in-phase symmetric stretching (ν_1), out-of-plane deformation (ν_2), asymmetric stretching (ν_3), and in-plane bending modes (ν_4), respectively. Three of the four modes are infrared active (ν_2, ν_3, and ν_4). In aqueous solution, the nitrate ion is perturbed enough such that all of these modes are infrared active. Furthermore, the ν_3 mode, which is degenerate in the gas phase, splits into a doublet in aqueous solution. The degree of this splitting ($\Delta\nu_3$) is dependent on the environment and thus perturbation of the nitrate ion. A highly perturbed ion will have a large splitting, whereas a relatively unperturbed ion will have a smaller value of $\Delta\nu_3$. In highly concentrated aqueous droplets, NO_3^- may be more likely to form contact-ion pairs by being in closer proximity to cations and thus increasing the splitting of the ν_3 absorbance band. Upon exposure to higher *RH*, the solution droplets take up water and become more dilute. It would be expected that this would lead to a decrease in $\Delta\nu_3$ because of greater separation between the NO_3^- ions and cations by water molecules.

The degree of splitting for each nitrate salt can be determined most easily from curve fitting the ν_3 absorption band into two bands with Gaussian line shapes, as shown in Figure 12. As the aqueous aerosol droplets become more dilute with increasing relative humidity $\Delta\nu_3$ decreases. The values of $\Delta\nu_3$ under low and high relative humidity conditions for $NaNO_3$, $Ca(NO_3)_2$, $Mg(NO_3)_2$, and the 1:1 calcium + magnesium nitrate mixture are summarized in Table 1. At higher relative humidity (near 60%), the degree of splitting decreases by 10−20 cm^{-1}. This suggests that the nitrate ions present in solution behave more like "free" ions as the aerosol droplets take up water and become more dilute. Previous studies of $Ca(NO_3)_2$ and $Mg(NO_3)_2$ have also shown that $\Delta\nu_3$ decreases as concentration decreases,[68,76] consistent with the result we obtain here.

On the basis of the WSR results discussed previously, it would be expected that $NaNO_3$ should exhibit the largest splitting because it has the least amount of water associated with each aerosol droplet. However, for $NaNO_3$ the splitting is not as evident as it is for the other nitrate aerosols. Instead, the spectra display a single peak with a broad shoulder, as shown in Figure 12a, to which the fits are applied. Cation effects explain the appearance of ν_3 as a single peak rather than a doublet in the $NaNO_3$ spectra. It has been shown that the ν_3 absorbance at high wavenumbers is more sensitive to changes in environment than the peak at lower wavenumbers.[77] The Na^+ ion only weakly affects the structure of NO_3^- in comparison to Ca^{2+} and Mg^{2+}.[77] The change in the value of $\Delta\nu_3$ for the divalent nitrate salts and the 1:1 mixture appears to have the same trend as the water-to-nitrate ion ratio, with $\Delta\nu_3$ changing the most for $Mg(NO_3)_2$ followed by 1:1 $Ca(NO_3)_2 + Mg(NO_3)_2$ and last $Ca(NO_3)_2$ with the smallest decrease in $\Delta\nu_3$.

At lower relative humidity, where the aerosol droplets are more concentrated, it is possible that contact-ion pairs may form between nitrate ions and the metal cations. Evidence for contact-ion pairing from IR and Raman studies has been suggested previously for highly concentrated $Ca(NO_3)_2$ solutions.[76,78] For $Mg(NO_3)_2$, it has been shown that contact-ion pairs form as the water content of a particle is decreased.[68,79] Although the formation of contact-ion pairs may be possible at low *RH* for each of the nitrate salts, we are unable to quantify the extent to which this may occur from our measured extinction spectra. This is due largely to overlap of the ν_3 absorption bands of a "free" nitrate ion and paired nitrate ion, making it difficult to distinguish one from the other.

For $NaNO_3$, the ν_1 band, an infrared inactive band for gas phase nitrate ion which is easily seen in the spectra for aqueous calcium nitrate and magnesium nitrate aerosols at all *RH* is barely visible at low *RH* and very weak at high *RH*. These data show clearly that the nitrate environment in the aerosol droplets change as a function of relative humidity. The extent of the perturbation will depend on the cation associated with the nitrate ion and the relative humidity. Therefore, the electronic and molecular structure of the nitrate ion will not only be *RH* dependent but will also vary with aerosol chemical composition.

Atmospheric and Climatic Impacts. The increased hygroscopicity of the nitrate salts that form as products of reactions with nitrogen oxides will lead to larger, more spherical aerosol particles because the particle will be aqueous over a wider range of relative humidity conditions. The highly hygroscopic nitrate salts will provide significant water content for heterogeneous reactions to occur at atmospherically relevant *RH*.

The significant difference in the CCN activity of 100 nm $CaCO_3$ and $Ca(NO_3)_2$ indicates that as mineral dust aerosol is transported and aged in the atmosphere its potential to act as CCN will increase dramatically. $Ca(NO_3)_2$ has a critical supersaturation (SS) comparable to that of $(NH_4)_2SO_4$, a large fraction of CCN in the atmosphere. At the same percent SS, $CaCO_3$ displays no CCN activity. The greater capacity for the aged aerosol, in comparison to freshly emitted mineral dust aerosol, to act as CCN will have a strong impact on indirect climate forcing. This work provides an important step in understanding how the changes in the physicochemical properties of mineral dust and sea salt aerosol due to chemical processing in the atmosphere will affect climate. Increased hygroscopicity and CCN activity of the mineral dust and sea salt aerosol will also result in greater cloud reflectivity and a decrease in precipitation efficiency.[80] To fully assess the impact of atmospheric aging on the climate forcing of mineral dust aerosol on a global scale, the use of detailed microphysical models is necessary.[81]

For each nitrate aerosol examined in this work, there is an increase in the scatter region from 4000 to 7000 cm^{-1} in the extinction spectra, signifying the presence of larger particles. In all cases, the relative amount of scattered light from 4000 to

7000 cm^{-1} is a factor of approximately three greater near 60% *RH* than at lower *RH*. In areas of high relative humidity, it is estimated that a highly hygroscopic particle may reflect 2−3 times more light than a dry particle.[82,83] Previous work has shown that the increase in the amount of light scattered by freshly emitted mineral dust aerosol (e.g., $CaCO_3$) is minimal as a $f(RH)$.[27] Furthermore, as discussed in the Introduction, the nitrate ion is known to absorb ultraviolet radiation near 300 nm. Thus the absorption of solar radiation by the aerosol will increase. On the basis of this knowledge, it is expected that mineral dust and sea salt aerosol that have undergone heterogeneous chemistry in the troposphere to form hygroscopic nitrate salts will have a significantly different impact on direct climate forcing than freshly emitted mineral dust and sea salt aerosol.

There is evidence that the single scattering albedo of mineral dust may increase as it is aged in the atmosphere because of enhanced water uptake by the products that form from reactions with nitrogen oxides.[84] Because the single scattering albedo is a key factor in assessing the impact of an aerosol on climate,[85] it is important to understand the physicochemical properties of mineral dust and sea salt aerosol as they are transported and aged in the atmosphere to fully quantify the effect they have on climate forcing.

Conclusions and Future Outlook

The results and data presented here show that physical chemistry measurements of atmospherically relevant aerosols are essential if aerosols, an important component of the Earth's atmosphere, can be fully understood. The studies presented here focus on single component nitrate salts and provide a first step forward in understanding how atmospheric aging of mineral dust and sea salt aerosol may impact climate. However, many additional interesting issues deserve further investigation. Suggestions for future studies include the following: (1) Reaction kinetics of the heterogeneous chemistry of nitrate aerosol with trace atmospheric gases (e.g., O_3, SO_2, HCOOH, OH) because the reactivity may be different than the original mineral dust or sea salt aerosol. (2) Measurements of the physical properties of complex nitrate mixtures with other components of atmospheric aerosol such as organics. The presence of an organic species may alter the hygroscopicity of the nitrate aerosol, thus affecting its impact on direct and indirect climate forcing. (3) Measurements of the physicochemical properties of multicomponent mineral dust aerosol that has been coated with a thin layer of nitrate, thus simulating partially atmospherically aged aerosol particles. The behavior of a coated particle is expected to be different than that of an uncoated mineral dust particle or a pure nitrate aerosol. (4) On the basis that photochemically inactive mineral dust and sea salt aerosol are readily converted to aqueous nitrate aerosols that are photochemically reactive, it is expected that as sea salt and mineral dust aerosol particles are transported, processed, and aged in the atmosphere they will become more photochemically reactive. Given that there is little known about the photolysis of NO_3^- in aqueous atmospheric aerosols, there is a need to further explore this potentially rich area. Future studies could include investigating the wavelength dependence of the photolysis reaction in the aqueous aerosol and the yields of NO_x and OH production. Furthermore, the changing nitrate environment in the aerosol droplets with *RH* indicate that these dependences (wavelength, yields, etc.) will be affected by how much water is associated with the aerosol and potentially by other constituents in the aerosol such as organics. Thus, it is concluded that fundamental molecular studies of atmospheric aerosols is a rich area for further study. Knowledge gleaned of aerosol properties on the molecular scale can lead to a greater understanding of the impact of aerosol properties on global scales.

Acknowledgment. This material is based upon work supported by the National Science Foundation under Grant No. 0503854. Any opinions, findings, and conclusions or recommendations expressed in this material are those of the author(s) and do not necessarily reflect the views of the National Science Foundation. We would like to thank Professor Paul Kleiber, Professor Mark Young, and Dr. Anthony Prenni for helpful discussions.

Appendix

The relationship between relative humidity and the equilibrium diameter of a droplet is described by Köhler theory.[48] For the calculation of theoretical growth curves, concentration- and temperature-dependent values of solution density, solution surface tension, and water activity are necessary. The methods used to determine these values for each salt are discussed in this section. For the growth curves calculated here, the temperature is 298 K. The density of pure water is calculated such that is equivalent to 0.997 g/cm^3 at 298 K. For the calculated Köhler growth curves displayed in Figures 4b, 6, and 9, it is assumed that the total mass and moles of each solute is equivalent to that of a dry 100 nm spherical particle and ρ_s is the bulk density of the nitrate salt.[15]

$(NH_4)_2SO_4$ Solutions. The theoretical growth curves (for both deliquescence and efflorescence) for $(NH_4)_2SO_4$ were calculated as described by Gysel et al. and through the use of the Aerosol Inorganics Model (AIM).[50,86] Water activities and their corresponding water-to-solute ratio were acquired directly from the online AIM model. Assuming volume additivity, the density of the solution droplet was calculated by linearly summing the weighted densities of bulk $(NH_4)_2SO_4$ and water.[49]

$$\rho_{sol} = \frac{1}{\frac{x}{\rho_s} + \frac{(1-x)}{\rho_w}} \quad \text{(A1)}$$

In eq A1, ρ_s is the density of the pure solute, x is the mass fraction of the solute, and ρ_w is the density of pure water. The particle diameter, D_p, is calculated assuming a sphere from the total volume of the solution droplet, which can be deduced from ρ_{sol} and the total droplet mass. D_p was calculated in this manner for each of the Köhler curves determined in this work. The surface tension of pure water (σ_w) as a function of temperature (°C)[47] is given by eq A2

$$\sigma_w(T) = 0.0761 - 1.55 \times 10^{-4} T \quad \text{(A2)}$$

The surface tension of the solution (in N/m) can then be calculated from

$$\sigma_{sol}(m_{salt}, T) = \sigma_w(T) + \beta_s m_{salt} \quad \text{(A3)}$$

where m_{salt} is the molality of the solution and β_s is a salt-specific coefficient, 2.17×10^{-3} N/m·M for $(NH_4)_2SO_4$.

$NaNO_3$ Solutions. The theoretical growth curve for $NaNO_3$ was also calculated as described by Gysel et al.[50] Briefly, the water activities for $NaNO_3$ are calculated through the use of eq A4

$$a_w = 1.0 - 5.52 \times 10^3 x + 1.286 \times 10^{-4} x^2 - 3.496 \times 10^{-6} x^3 + 1.843 \times 10^{-8} x^4 \quad \text{(A4)}$$

TABLE 2: Coefficients for the Calculation of Molality at Given Water Activities for $Ca(NO_3)_2$ and $Mg(NO_3)_2$

	a_0	a_1	a_2	a_3	a_4	a_5
$Ca(NO_3)_2$[a]	36.356	−165.66	447.46	−673.55	510.91	−155.56
$Mg(NO_3)_2$[b]	12.1658	−16.1538	0	10.8864	0	−6.8151

[a] Kelly and Wexler, 2005 (ref 81). [b] Ha and Chan, 2002 (ref 60).

where x is the $NaNO_3$ mass percentage.[52] Solution densities (ρ_{sol}) are determined up to high supersaturations by

$$\rho_{sol}(T,x) = \rho_w(T) + \sum_i A_i x^i \quad \text{(A5)}$$

where again, x is the $NaNO_3$ concentration in mass percent, ρ_w is the density of pure water, and A_i are salt-specific coefficients.[87] The solution surface tension was calculated from eqs A2 and A3, where β_s is equal to 1.12×10^{-3} N/m·M for $NaNO_3$.[88]

$Ca(NO_3)_2$ and $Mg(NO_3)_2$ Solutions. The Köhler curves for $Ca(NO_3)_2$ and $Mg(NO_3)_2$ were calculated using eqs 13 and 14. The values of the water activity (a_w) used to calculate the theoretical growth of these two nitrates are assumed to range from 0.01 to 1. Given a specific water activity, the molality of a solution is given by

$$m(a_w) = a_0 + a_1 a_w + a_2 a_w^2 + a_3 a_w^3 + a_4 a_w^4 + a_5 a_w^5 \quad \text{(A6)}$$

This fit is applicable for values of a_w greater than approximately 0.15 and 0.28 for $Ca(NO_3)_2$ and $Mg(NO_3)_2$, respectively,[67,89] but we have extrapolated it to include our entire relative humidity range. The values of the coefficients used for $Ca(NO_3)_2$ and $Mg(NO_3)_2$ are given in Table 2.[67,89] Assuming a dry diameter of 100 nm and a known bulk crystal density, the moles of solute can be determined and used to calculate the moles of water in a droplet from the molality. Knowing the moles of solute and water, the mass fraction of each can be calculated and used to determine the density of the droplet from eq A1. Weissenborn and Pugh have measured the change in the surface tension of water ($\Delta\sigma_w$) upon the addition of $Ca(NO_3)_2$ or $Mg(NO_3)_2$.[90] By applying a linear fit to their data, we are able to determine a relationship between $\Delta\sigma_w$ and molarity. Molarity is easily determined from the droplet volume and known solute moles. The value of σ_{sol} at a given droplet concentration can then be determined from the sum of σ_w (calculated according to eq A2) and $\Delta\sigma_w$.

1:1 Calcium + Magnesium Nitrate Mixture. To calculate the theoretical growth curve for the 1:1 calcium + magnesium nitrate mixture, we have assumed that the dry composition of the mixed particle is $CaMg(NO_3)_4$ and its bulk density is an average of ρ_s for pure $Ca(NO_3)_2$ and $Mg(NO_3)_2$. Water activity data and corresponding solute mass fractions for $a_w > 0.20$ for the nitrate mixture were taken from recent work by Choi and Chan.[91] The density of the mixed solution droplet was calculated using eq A1. To our knowledge, there are no literature data available for the surface tension of $Ca(NO_3)_2$ and $Mg(NO_3)_2$ mixtures. By taking an average of the linear fits applied to the data presented by Weissenborn and Pugh for the pure salts, we have determined a relationship between $\Delta\sigma_w$ and molarity for the nitrate mixture.[90] As for the pure salts, the sum of σ_w and $\Delta\sigma_w$ was used in eq 13 as σ_{sol}.

References and Notes

(1) Usher, C. R.; Michel, A. E.; Grassian, V. H. *Chem. Rev.* **2003**, *103*, 4883−4939.

(2) Finlayson-Pitts, B. J. *Chem. Rev.* **2003**, *103*, 4801−4822.

(3) Bian, H.; Zender, C. S. *J. Geophys. Res.* **2003**, *108*, 4672, doi: 10.1029/2002JD003143.

(4) Tang, Y.; Carmichael, G. R.; Kurata, G.; Uno, I.; Weber, R. J.; Song, C.-H.; Guttikunda, S. K.; Woo, J.-H.; Streets, D. G.; Wei, C.; Clarke, A. D.; Huebert, B.; Anderson, T. L. *J. Geophys. Res.* **2004**, *109*, D19S21, doi: 10.1029/2003JD003806.

(5) Song, C. H.; Carmichael, G. R. *J. Atmos. Chem.* **2001**, *40*, 1−22.

(6) de Reus, M.; Fischer, H.; Sander, R.; Gros, V.; Kormann, R.; Salisbury, G.; Van Dingenen, R.; Williams, J.; Zoellner, M.; Lelieveld, J. *Atmos. Chem. Phys.* **2005**, *5*, 1787−1803.

(7) Martin, R. V.; Jacob, D. J.; Yantosca, R. M.; Chin, M.; Ginoux, P. *J. Geophys. Res.* **2003**, *108*, 4097, doi: 10.1029/2002JD002622.

(8) Liao, H.; Seinfeld, J. H.; Adams, P. J.; Mickley, L. J. *J. Geophys. Res.* **2004**, *109*, D16207, doi: 10.1029/2003JD004456.

(9) Bauer, S. E.; Balkanski, Y.; Schulz, M.; Hauglustaine, D. A.; Dentener, F. *J. Geophys. Res.* **2004**, *109*, D02304, doi: 10.1029/2003JD003868.

(10) Song, C. H.; Carmichael, G. R. *J. Geophys. Res.* **2001**, *106*, 18131, doi: 10.1029/2000JD900352.

(11) Finlayson-Pitts, B. J.; Hemminger, J. C. *J. Phys. Chem. A* **2000**, *104*, 11463−11477.

(12) Hoffman, R. C.; Kaleuati, M. A.; Finlayson-Pitts, B. J. *J. Phys. Chem. A* **2003**, *107*, 7818−7826.

(13) Hoffman, R. C.; Gebel, M. E.; Fox, B. S.; Finlayson-Pitts, B. J. *Phys. Chem. Chem. Phys.* **2003**, *5*, 1780−1789.

(14) Vogt, R.; Finlayson-Pitts, B. J. *J. Phys. Chem.* **1994**, *98*, 3747−55.

(15) *CRC Handbook of Chemistry and Physics*, Internet Version 2006, http://www.hbcpnetbase.com, 86th ed.; Taylor and Francis: Boca Raton, FL, 2006.

(16) Krueger, B. J.; Grassian, V. H.; Cowin, J. P.; Laskin, A. *Atmos. Environ.* **2004**, *38*, 6253−6261.

(17) Krueger, B. J.; Grassian, V. H.; Cowin, J. P.; Laskin, A. *Atmos. Environ.* **2005**, *39*, 395.

(18) Krueger, B. J.; Grassian, V. H.; Laskin, A.; Cowin, J. P. *Geophys. Res. Lett.* **2003**, *30*, 1148, doi: 10.1029/2002GL016563.

(19) Laskin, A.; Wietsma, T. W.; Krueger, B. J.; Grassian, V. H. *J. Geophys. Res.* **2005**, *110*, D10208, doi:10.1029/2004JD005206.

(20) Krueger, B. J.; Grassian, V. H.; Iedema, M. J.; Cowin, J. P.; Laskin, A. *Anal. Chem.* **2003**, *75*, 5170.

(21) Mogili, P. K.; Kleiber, P. D.; Young, M. A.; Grassian, V. H. *Atmos. Environ.*, in press, 2006.

(22) Dentener, F. J.; Carmichael, G. R.; Zhang, Y.; Lelieveld, J.; Crutzen, P. J. *J. Geophys. Res.* **1996**, *101*, 22869, doi: 10.1029/96JD01818.

(23) Ooki, A.; Uematsu, M. *J. Geophys. Res.* **2005**, *110*, D03201, doi: 10.1029/2004JD004737.

(24) Laskin, A.; Iedema, M. J.; Ichkovich, A.; Graber, E. R.; Taraniuk, I.; Rudich, Y. *Faraday Discuss.* **2005**, *130*, 453.

(25) Matsuki, A.; Iwasaka, Y.; Shi, G.; Zhang, D.; Trichkine, D.; Yamada, M.; Kim, Y. S.; Chen, B.; Nagatani, T.; Miyazawa, T.; Nagatani, M.; Nakata, H. *Geophys. Res. Lett.* **2005**, *32*, doi: 10.1029/2005GL024176.

(26) Sullivan, R. C.; Guazzotti, S. A.; Sodeman, D. A.; Prather, K. A. *Atmos. Chem. Phys. Discuss.* **2006**, *6*, 4109−4170.

(27) Gibson, E. R.; Hudson, P. K.; Grassian, V. H. *Geophys. Res. Lett.* **2006**, *33*, L13811, doi: 10.1029/2006GL026386.

(28) Kalashnikova, O. V.; Kahn, R.; Sokolik, I. N.; Li, W. H. *J. Geophys. Res.* **2005**, *110*, D18S14, doi: 10.1029/2004JD004550.

(29) Pilinis, C.; Pandis, S. N.; Seinfeld, J. H. *J. Geophys. Res.* **1995**, *100*, 18739, doi: 10.1029/95JD02119.

(30) Garrett, T. J.; Russell, L. M.; Ramaswamy, V.; Maria, S. F.; Huebert, B. J. *J. Geophys. Res.* **2003**, *108*, 4022, doi: 10.1029/2002JD002228.

(31) Ravishankara, A. R. *Faraday Discuss.* **2005**, *130*, 9.

(32) Honrath, R. E.; Peterson, M. C.; Guo, S.; Dibb, J. E.; Shepson, P. B.; Campbell, B. *Geophys. Res. Lett.* **1999**, *26*, 695, doi: 10.1029/1999GL900077.

(33) Young, M. A. Environmental Photochemistry in Surface Waters. In *Water Encyclopedia: Oceanography; Meteorology; Physics and Chemistry; Water Law; and Water History, Art, and Culture*; Lehr, J. H., Keeley, J., Eds.; John Wiley and Sons: New York, 2005.

(34) Chu, L.; Anastasio, C. *J. Phys. Chem. A* **2003**, *107*, 9594−9602.

(35) Daniels, M.; Meyers, R. V.; Belardo, E. V. *J. Phys. Chem.* **1968**, *72*, 389−399.

(36) Dubowski, Y.; Colussi, A. J.; Hoffmann, M. R. *J. Phys. Chem. A* **2001**, *105*, 4928−4932.

(37) Mack, J.; Bolton, J. R. *J. Photochem. Photobiol., A* **1999**, *128*, 1−14.

(38) Mark, G.; Korth, H.-G.; Schuchmann, H.-P.; von Sonntag, C. *J. Photochem. Photobiol., A* **1996**, *101*, 89−103.

(39) Warneck, P.; Wurzinger, C. *J. Phys. Chem.* **1988**, *92*, 6278−83.

(40) Zellner, R.; Exner, M.; Herrmann, H. *J. Atmos. Chem.* **1990**, *10*, 411−425.

(41) Honrath, R. E.; Guo, S.; Peterson, M. C.; Dziobak, M. P.; Dibb, J. E.; Arsenault, M. A. *J. Geophys. Res.* **2000**, *105*, 24183, doi: 10.1029/2000JD900361.
(42) Honrath, R. E.; Peterson, M. C.; Dziobak, M. P.; Dibb, J. E.; Arsenault, M. A.; Green, S. A. *Geophys. Res. Lett.* **2000**, *27*, 2237, doi: 10.1029/1999GL011286.
(43) Jones, A. E.; Weller, R.; Minikin, A.; Wolff, E. W.; Sturges, W. T.; McIntyre, H. P.; Leonard, S. R.; Schrems, O.; Bauguitte, S. *J. Geophys. Res.* **1999**, *104*, 21355, doi: 10.1029/1999JD900362.
(44) Jones, A. E.; Weller, R.; Wolff, E. W.; Jacobi, H. W. *Geophys. Res. Lett.* **2000**, *27*, 345, doi: 10.1029/1999GL010885.
(45) Ridley, B.; Walega, J.; Montzka, D.; Grahek, F.; Atlas, E.; Flocke, F.; Stroud, V.; Deary, J.; Gallant, A.; Boudries, H.; Bottenheim, J.; Anlauf, K.; Worthy, D.; Sumner, A. L.; Splawn, B.; Shepson, P. *J. Atmos. Chem.* **2000**, *36*, 1−22.
(46) Roberts, G.; Nenes, A. *Aerosol Sci. Technol.* **2005**, *39*, 206−221.
(47) Seinfeld, J. H.; Pandis, S. N. *Atmospheric Chemistry and Physics: From Air Pollution to Climate Change*; John Wiley & Sons: New York, 1998.
(48) Kohler, H. *Trans. Faraday Soc.* **1936**, *32*, 1152−61.
(49) Kreidenweis, S. M.; Koehler, K.; DeMott, P. J.; Prenni, A. J.; Carrico, C.; Ervens, B. *Atmos. Chem. Phys.* **2005**, *5*, 1357.
(50) Gysel, M.; Weingartner, E.; Baltensperger, U. *Environ. Sci. Technol.* **2002**, *36*, 63.
(51) Onasch, T. B.; Siefert, R. L.; Brooks, S. D.; Prenni, A. J.; Murray, B.; Wilson, M. A.; Tolbert, M. A. *J. Geophys. Res.* **1999**, *104*, 21317, doi: 10.1029/1999JD900384.
(52) Tang, I. N.; Munkelwitz, H. R. *J. Geophys. Res.* **1994**, *99*, 18801, doi: 10.1029/94JD01345.
(53) Tang, I. N.; Munkelwitz, H. R. *Atmos. Environ.* **1993**, *27A*, 467−473.
(54) Tang, I. N.; Fung, K. H.; Imre, D. G.; Munkelwitz, H. R. *Aerosol Sci. Technol.* **1995**, *23*, 443−453.
(55) Cziczo, D. J.; Nowak, J. B.; Hu, J. H.; Abbatt, J. P. D. *J. Geophys. Res.* **1997**, *102*, 18843, doi: 10.1029/97JD01361.
(56) Hoffman, R. C.; Laskin, A.; Finlayson-Pitts, B. J. *J. Aerosol Sci.* **2004**, *35*, 869−887.
(57) Lee, C.-T.; Hsu, W.-C. *J. Aerosol Sci.* **1999**, *31*, 189−197.
(58) McInnes, L. M.; Quinn, P. K.; Covert, D. S.; Anderson, T. L. *Atmos. Environ.* **1996**, *30*, 869−884.
(59) Al-Hosney, H. A.; Grassian, V. H. *Phys. Chem. Chem. Phys.* **2005**, *7*, 1266.
(60) Gustafsson, R. J.; Orlov, A.; Badger, C. L.; Griffiths, P. T.; Cox, R. A.; Lambert, R. M. *Atmos. Chem. Phys. Discuss.* **2005**, *5*, 7191.
(61) Tang, I. N.; Fung, K. H. *J. Chem. Phys.* **1997**, *106*, 1653.
(62) Ishizaka, Y.; Adhikari, M. *J. Geophys. Res.* **2003**, *108*, 4138, doi: 10.1029/2002JD002085.
(63) Twomey, S. *J. Atmos. Sci.* **1971**, *28*, 377.
(64) Al-Abadleh, H. A.; Grassian, V. H. *J. Phys. Chem. B* **2003**, *107*, 10829−10839.
(65) Weis, D. D.; Ewing, G. E. *J. Phys. Chem. A* **1999**, *103*, 4865−4873.
(66) Al-Abadleh, H. A.; Krueger, B. J.; Ross, J. L.; Grassian, V. H. *Chem. Commun.* **2003**, 2796.
(67) Ha, Z.; Chan, C. K. *Aerosol Sci. Technol.* **1999**, *31*, 154−169.
(68) Zhang, Y.-H.; Choi, M. Y.; Chan, C. K. *J. Phys. Chem. A* **2004**, *108*, 1712−1718.
(69) Choi, M. Y.; Chan, C. K. *J. Phys. Chem. A* **2005**, *109*, 1042−1048.
(70) El Guendouzi, M.; Marouani, M. *J. Solution Chem.* **2003**, *32*, 535−546.
(71) Chan, C. K.; Zhang, Y.-H. Personal communication.
(72) Burgess, J. *Metal Ions in Solution*; Ellis Horwood: Chichester, England, 1978.
(73) Downing, H. D.; Williams, D. *J. Geophys. Res.* **1975**, *80*, 1656−60.
(74) Sporleder, D.; Ewing, G. E. *J. Phys. Chem. A* **2001**, *105*, 1838−1846.
(75) Frinak, E. K.; Mashburn, C. D.; Tolbert, M. A.; Toon, O. B. *J. Geophys. Res.* **2005**, *110*, D09308, doi: 10.1029/2004JD005647.
(76) Irish, D. E.; Walrafen, G. E. *J. Chem. Phys.* **1967**, *46*, 378.
(77) Liu, J.-H.; Zhang, Y.-H.; Wang, L.-Y.; Wei, Z.-F. *Spectrochim. Acta, Part A* **2005**, *61*, 893−899.
(78) Hester, R. E.; Plane, R. A. *J. Chem. Phys.* **1964**, *40*, 411−414.
(79) Chang, T. G.; Irish, D. E. *J. Phys. Chem.* **1973**, *77*, 52−57.
(80) Lohmann, U.; Feichter, J. *Atmos. Chem. Phys. Discuss.* **2005**, *5*, 715.
(81) Conant, W. C.; Seinfeld, J. H.; Wang, J.; Carmichael, G. R.; Tang, Y.; Uno, I.; Flatau, P. J.; Markowicz, K. M.; Quinn, P. K. *J. Geophys. Res.* **2003**, *108*, 8661, doi: 10.1029/2002JD003260.
(82) Day, D. E.; Malm, W. C.; Kreidenweis, S. M. *J. Air Waste Manage.* **2000**, *50*, 710.
(83) McInnes, L.; Bergin, M.; Ogren, J.; Schwartz, S. *Geophys. Res. Lett.* **1998**, *25*, 513, doi: 10.1029/98GL00127.
(84) Vlasenko, A.; Sjogren, S.; Weingartner, E.; Stemmler, K.; Gaggeler, H. W.; Ammann, M. *Atmos. Chem. Phys. Discuss.* **2005**, *5*, 11821.
(85) Seinfeld, J. H.; Carmichael, G. R.; Arimoto, R.; Conant, W. C.; Brechtel, F. J.; Bates, T. S.; Cahill, T. A.; Clarke, A. D.; Doherty, S. J.; Flatau, P. J.; Huebert, B. J.; Kim, J.; Markowicz, K. M.; Quinn, P. K.; Russell, L. M.; Russell, P. B.; Shimizu, A.; Shinozuka, Y.; Song, C. H.; Tang, Y.; Uno, I.; Vogelmann, A. M.; Weber, R. J.; Woo, J.-H.; Zhang, X. Y. *Bull. Am. Meteor. Soc.* **2004**, *85*, 367.
(86) Clegg, S. L.; Brimblecombe, P.; Wexler, A. S. *J. Phys. Chem. A* **1998**, *102*, 2155−2171.
(87) Tang, I. N. *J. Geophys. Res.* **1997**, *102 (D2)*, 1883−1894, doi: 10.1029/96JD03085.
(88) Chen, J.-P. *J. Atmos. Sci.* **1994**, *51*, 3505−3516.
(89) Kelly, J. T.; Wexler, A. S. *J. Geophys. Res.* **2005**, *110*, D11201, doi: 10.1029/2004JD005583.
(90) Weissenborn, P. K.; Pugh, R. J. *J. Colloid Interface Sci.* **1996**, *184*, 550.
(91) Choi, M. Y.; Chan, C. K. *J. Chem. Eng. Data* **2002**, *47*, 1526−1531.